Evaluating Clouds in Long-Term Cloud-Resolving Model Simulations with Observational Data

XIPING ZENG,*,+ WEI-KUO TAO,+ MINGHUA ZHANG,# CHRISTA PETERS-LIDARD,@ STEPHEN LANG,+,& JOANNE SIMPSON,+ SUJAY KUMAR,*,@ SHAOCHENG XIE,** JOSEPH L. EASTMAN,*,@ CHUNG-LIN SHIE,*,+ AND JAMES V. GEIGER@

* *Goddard Earth Sciences and Technology Center, University of Maryland, Baltimore County, Baltimore, Maryland*
+ *Laboratory for Atmospheres, NASA Goddard Space Flight Center, Greenbelt, Maryland*
# *Marine Sciences Research Center, Stony Brook University, Stony Brook, New York*
@ *Laboratory for Hydrospheric Processes, NASA Goddard Space Flight Center, Greenbelt, Maryland*
& *Science Systems and Applications, Inc., Lanham, Maryland*
** *Atmospheric Sciences Division, Lawrence Livermore National Laboratory, Livermore, California*

(Manuscript received 15 May 2006, in final form 13 February 2007)

ABSTRACT

Two 20-day, continental midlatitude cases are simulated with a three-dimensional (3D) cloud-resolving model (CRM) and are compared to Atmospheric Radiation Measurement Program (ARM) data. Surface fluxes from ARM ground stations and a land data assimilation system are used to drive the CRM. This modeling evaluation shows that the model simulates precipitation well but overpredicts clouds, especially in the upper troposphere. The evaluation also shows that the ARM surface fluxes can have noticeable errors in summertime.

Theoretical analysis reveals that buoyancy damping is sensitive to spatial smoothers in two-dimensional (2D) CRMs, but not in 3D ones. With this theoretical analysis and the ARM cloud observations as background, 2D and 3D simulations are compared, showing that the 2D CRM has not only rapid fluctuations in surface precipitation but also spurious dehumidification (or a decrease in cloud amount). The present study suggests that the rapid precipitation fluctuation and spurious dehumidification be attributed to the sensitivity of buoyancy damping to dimensionality.

1. Introduction

a. Motivation

The representation of clouds in general circulation models (GCMs) is one of the most important challenges in simulating the global water and energy cycle (e.g., Cess et al. 1990; Zhang et al. 2005). Currently, cloud-resolving models (CRMs) are being incorporated into large-scale dynamic frameworks (e.g., GCMs) to facilitate the interaction between clouds and large-scale circulations in place of conventional cumulus parameterization (Emanuel and Raymond 1993) as an alternative approach (e.g., Grabowski 2001; Khairoutdinov and Randall 2001; Raymond and Zeng 2005; Khairoutdinov et al. 2005; Chern et al. 2005, unpublished manuscript). This approach is referred to as a superparameterization or multiscale modeling framework (MMF; Randall et al. 2003). The approach has merit, since no assumption is introduced on the causality between cumulus clouds and large-scale circulations. A key question is whether current CRMs can function in an MMF as expected. This question can be addressed by evaluating long-term CRM simulations against observations. Here long-term simulation means a period comparable to the long time scale in the approach to radiative–convective equilibrium (Tompkins and Craig 1998), which is around three weeks.

Consider a CRM in an ideal MMF with no computational limits. The CRM can represent clouds in a computationally expensive way [e.g., a three-dimensional (3D) framework with sufficient grid points]. When the CRM is driven with prescribed large-scale forcing, the difference between the modeling results and observations is attributed to model physics instead of computational issues [e.g., a two-dimensional (2D) framework

Corresponding author address: Dr. Xiping Zeng, Mail Code 613.1, NASA Goddard Space Flight Center, Greenbelt, MD 20771.
E-mail: zeng@agnes.gsfc.nasa.gov

DOI: 10.1175/2007JAS2170.1

© 2007 American Meteorological Society

or insufficient grid points]. Thus, the difference between the modeling results and observations provides insights on improving the CRMs used in MMFs. In this direction, the Goddard Cumulus Ensemble (GCE) model is evaluated with data collected in the Atmospheric Radiation Measurement Program (ARM). Two 20-day, continental midlatitude cases were selected for this purpose.

b. Model evaluation

CRM evaluation can be traced back two decades. Although real clouds and cloud systems are 3D, most CRMs used today are still 2D due to computer resources (Krueger 1988; Xu and Randall 1996; Wu et al. 1998; Li et al. 1999; Liu and Moncrieff 2004; and many others). Only a few 3D CRMs (e.g., Tao and Soong 1986; Lipps and Hemler 1986) have been used to study the response of clouds to large-scale forcing. Previous studies showed that the collective thermodynamic feedback effect and the vertical transports of mass, sensible heat, and moisture were similar between 2D and 3D simulations in the life cycle of individual clouds (e.g., Tao et al. 1987). Recently, several 3D CRM experiments were performed for 7-day periods for tropical cloud systems with large horizontal domains (500×500 km^2) at the National Center for Atmospheric Research (Grabowski et al. 1998; Wu et al. 1998), National Oceanic and Atmospheric Administration/Geophysical Fluid Dynamics Laboratory (NOAA/GFDL; Donner et al. 1999), Met Office (Petch and Gray 2001), Colorado State University (Khairoutdinov and Randall 2003), and National Aeronautics and Space Administration (NASA) Goddard Space Flight Center (Tao 2003).

In the present study, the 3D GCE model is used to simulate continental midlatitude clouds for twenty days, longer than most previous 3D CRM simulations, to evaluate the simulated cloud residues (i.e., cloud ice, cloud water and water vapor). Cloud residues are a natural consequence of cloud growth. Since surface precipitation rate can be regarded as a measure of cloud growth, temporal and accumulated modeled surface precipitation is compared with the observed first. Special attention is paid here to the sensitivity of clouds to dimensionality.

Model evaluation depends strongly on observational data quality (Moncrieff et al. 1997). Some recent field experiments [e.g., the ARM Spring 2000 Intensive Operational Period (IOP) and the ARM International H_2O Project (IHOP) in 2002] have provided comprehensive observational data (e.g., Ackerman and Stokes 2003; Weckwerth et al. 2004) for model evaluation. The observed cloud properties from the ARM Spring 2000 IOP, for example, are the best in the 14-yr history of the ARM program (Xu et al. 2005).

This study involves two 20-day observation periods during two field experiments. One is from the ARM 2000 IOP and the other IHOP 2002. Some of the cloud systems in these experiments have already been studied for specific purposes, such as the life cycle of convective clouds and as a setting for a model intercomparison (Wakimoto et al. 2004; Xie et al. 2005; Xu et al. 2005). Xie et al. (2005) and Xu et al. (2005) focused on two short periods within the ARM 2000 IOP to compare four 2D CRMs as well as eight single-column models with observations. They suggested that 3D CRM simulations be done to narrow down the origins of differences between the 2D CRMs and observations.

c. Dimensionality sensitivity of clouds

Suppose that cloud properties in CRMs are sensitive to dimensionality. Thus, cloud–radiation interaction in MMFs should be sensitive to CRM dimensionality, because cloud properties affect atmospheric radiation, which in turn impacts the large-scale circulation (e.g., Albrecht and Cox 1975; Raymond 2000; Raymond and Zeng 2000), which in turn modifies the clouds to complete the feedback (Raymond and Zeng 2005).

In fact, previous studies (e.g., Grabowski et al. 1998; Donner et al. 1999; Tompkins 2000; Khairoutdinov and Randall 2003; Petch and Gray 2001; Phillips and Donner 2006) showed contrary conclusions on the sensitivity of CRM cloud properties to dimensionality, although they all showed that precipitation rate fluctuates more rapidly in 2D CRMs than in their 3D counterparts. Grabowski et al. (1998) showed that the 7-day mean cloud fractions were very close between their 2D and 3D CRMs, which was supported by Tompkins (2000) and Khairoutdinov and Randall (2003). In contrast, Donner et al. (1999) and Phillips and Donner (2006) found significantly larger ice contents in the upper troposphere in their 3D CRM than in its 2D counterpart. Petch and Gray (2001) used two different microphysics parameterizations and got quite different results. Using an older version (Swann 1998), they got results that supported Grabowski et al. (1998). But, with a newer scheme based on Brown and Heymsfield (2001), they got results to support Donner et al. (1999) and Phillips and Donner (2006).

However, no explanation was available up until now to rectify those contrary conclusions (see section 5b for a discussion). But, by combining numerical experiments, cloud observations, and theoretical analysis, the present paper addresses the sensitivity of cloud properties to dimensionality and explains how cloud model structure influences cloud simulations through cloud

microphysics parameterization. The paper is organized as follows. Section 2 describes the models and observational data used. Section 3 analyzes the modeling results for springtime cloud systems and compares 2D and 3D simulations to examine the sensitivity of cloud properties to dimensionality. Section 4 analyzes the modeling results for summertime cloud systems and tests the sensitivity of clouds to surface fluxes. Section 5 discusses the influence of cloud model structure on cloud properties through cloud microphysics parameterization as a summary, explaining the sensitivity of clouds to dimensionality. Finally, section 6 provides a brief set of conclusions.

2. Design of numerical experiments

a. CRM description

A single-column CRM, which differs from the two-column models designed to account for the interaction between convection and large-scale circulations (Nilsson and Emanuel 1999; Sobel and Bretherton 2000; Raymond and Zeng 2000, 2005), is used here to test the response of clouds to prescribed large-scale forcing derived from observational data. Experiment setup follows previous ones (e.g., Johnson et al. 2002; Xie et al. 2005; Xu et al. 2005) except for surface flux input. In the current framework, clouds are simulated with the GCE model, large-scale forcing data come from observations, and surface fluxes in the lower boundary come from either observations or a land data assimilation system.

The GCE model is detailed in Tao and Simpson (1993) and Tao et al. (2003), which describes its development and main features. Its application to studies of precipitation processes and improving satellite retrievals can be found in Simpson and Tao (1993) and Tao (2003). The model is nonhydrostatic and anelastic. It can be used in two or three dimensions with cyclic lateral boundary conditions. Solar and infrared radiative transfer processes (two-stream discrete-ordinate scattering) are included. Their impact on cloud development associated with cloud–radiation interaction has been assessed (Tao et al. 1996). Subgrid-scale (turbulent) processes in the model are parameterized using a scheme based on Klemp and Wilhelmson (1978) and Soong and Ogura (1980). The effects of both dry and moist processes on the generation of subgrid-scale kinetic energy have been incorporated. A three-class ice formulation (3ICE), namely that by Lin et al. (1983), was used. The sedimentation of ice crystals was recently included in the GCE based on Heymsfield and Donner (1990) and Heymsfield and Iaquinta (2000) and was discussed in detail in Hong et al. (2004). All scalar variables (temperature, water vapor, and all hydrometeors) are calculated with a positive definite advection scheme (Smolarkiewicz and Grabowski 1990). Results from the positive definite advection scheme are in better agreement with observations for tropical cloud systems (Johnson et al. 2002).

b. Land data assimilation system description

In addition to the ARM surface fluxes, for land surface sensitivity experiments, the surface fluxes were extracted from the Land Information System (LIS; Kumar et al. 2006). LIS is a high-performance land surface modeling and data assimilation system. It contains numerous land surface models (LSMs) that can be driven by a variety of atmospheric forcing from point to gridded data. For this study the NOAH LSM was employed. This LSM simulates soil moisture (both liquid and frozen), soil temperature, skin temperature, snowpack depth, snowpack water equivalent (and hence snowpack density), canopy water content, and the energy flux and water flux terms of the surface energy and surface water balances. The LSM land surface parameters were initialized with University of Maryland 1-km datasets for vegetation and land–sea masks (Hansen et al. 2000). Climatological datasets were ingested in order to initialize other vegetation parameters such as albedo and green vegetation fraction. Soils types were set using the State Soil Geographic Database for State (Soil Survey Staff 2006), which has a 1-km horizontal resolution. Initial soil water and temperature profiles were also assigned according to climatology.

The LSM was integrated for 15 yr up through the study period. For the period 1985 through 1996, National Centers for Environmental Prediction (NCEP) reanalysis data [the NCEP reanalysis data were obtained from the NOAA–Cooperative Institute for Research in Environmental Sciences (CIRES) Earth System Research Laboratory/Physical Sciences Division (ESRL/PSD) Climate Diagnostics Branch, Boulder, Colorado (see online at http://www.cdc.noaa.gov/)] were used for the atmospheric forcing. After this period, ⅛° atmospheric forcing was provided by the North American Land Data Assimilation System (NLDAS; Cosgrove et al. 2003), which incorporates high-resolution Geostationary Operational Environmental Satellite (GOES) radiation and stage IV precipitation fields into the NCEP Eta Data Assimilation System (EDAS). Modeled fluxes and temperature fields were then evaluated against a variety of surface station data and found to be in excellent agreement with observations. The modeled latent and sensible heat fluxes were then extracted for use in the GCE model.

TABLE 1. List of numerical experiments for cases.

Experiment name	Period	Dimension	Grid size	Grid point	Surface flux	Comments
C00	1–20 Mar 2000	3	1 km	128 × 128 × 41	ARM	Control run for case 2000
D00	1–20 Mar 2000	2	1 km	512 × 41	ARM	Dimensionality sensitivity
C02	25 May–13 Jun 2002	3	1 km	128 × 128 × 41	ARM	Control run for case 2002
L02	25 May–13 Jun 2002	3	1 km	128 × 128 × 41	LIS	Land surface flux sensitivity

c. *ARM observational data*

Two cases are studied in the present paper. The first one is the ARM Spring 2000 IOP, which was also used in the ARM Cloud Parameterization and Modeling Working Group (CPM WG) Case 4 study (Xie et al. 2005; Xu et al. 2005). This dataset starts at 1730 UTC 1 March and ends at 0830 UTC 22 March 2000. The second case covers the period from 2030 UTC 25 May to 830 UTC 14 June 2002 for the same ARM domain, which overlaps IHOP 2002. The two cases represent springtime and summertime midlatitude clouds, respectively.

The ARM observational data used are classified into two parts: forcing and evaluation data. Large-scale forcing data (i.e., vertical motion and horizontal advective tendencies of temperature and moisture) are derived using data collected from the two ARM IOPs and the variational analysis approach described in Zhang and Lin (1997) and Zhang et al. (2001). The values represent the mean ARM Cloud and Radiation Test Bed (CART) domain rather than a single point (Zhang et al. 2001). The surface fluxes are obtained from site-wide averages of observed fluxes from the ARM Energy Balance Bowen Ratio (EBBR) stations. The fluxes are assumed to be horizontally uniform in the model. The LIS fluxes, which provide an alternate source for surface fluxes, are used for comparison and are discussed in section 4b as well as in the preceding subsection.

Evaluation data include observed temperature and humidity as well as liquid and ice water contents and cloud fraction. Temperature and humidity are observed every three hours during the IOPs. Cloud liquid water content and ice water content are obtained as ARM "Microbase" products (Miller et al. 2003). Vertical profiles of cloud fraction are derived from the hydrometeor frequencies from the Active Remotely Sensed Cloud Layers (ARSCL) data archive (Clothiaux et al. 2000). The uncertainties in those quantities were discussed by Xie et al. (2005).

d. *A quick survey of numerical experiments*

A default numerical experiment is set up with a 1-km horizontal resolution, vertical resolution that ranges from 42.5 m at the bottom to 1 km at the top, and an integration time step of 6 s. A sponge layer aloft is introduced with a strength of $k(z - z_0)$, where $z_0 = 10$ km and $k = 2.1 \times 10^{-6}$ km^{-1} s^{-1} is constant above the height $z = 15.5$ km. The Lin et al. (1983) microphysics are used. The cloud model uses 128 × 128 × 41 grid points and is integrated for 20 days except for specific tests. The model domain is located over the ARM Southern Great Plains (SGP) site with the center at 36.6°N, 96.5°W.

The numerical experiments discussed in the paper are listed in Table 1 for quick reference. Two control experiments C00 and C02 are designed for the 2000 and 2002 cases, respectively. The first one, C00, simulates springtime clouds in 2000 to address the sensitivity of clouds to atmospheric factors. It uses 128 × 128 × 41 grid points at 1-km horizontal resolution and the surface fluxes from the ARM observations (Fig. 1). A 2D experiment, D00, is used to assess the sensitivity of clouds to dimensionality.

The other control experiment, C02, simulates summertime clouds in 2002 to examine the sensitivity of clouds to surface fluxes. It uses the same model parameters as C00 and the surface fluxes from the ARM observations (the upper part of Fig. 2). As shown by Figs. 1 and 2, the 2002 case possesses stronger surface latent heat flux both in amplitude and daily average than the 2000 case. In contrast to C02, experiment L02 uses surface fluxes from LIS, a land data assimilation system, that are then averaged horizontally for comparison. A snapshot of the spatial distribution of the LIS surface fluxes at day 1 is shown in Fig. 3. The horizontally averaged surface fluxes are also shown in the lower part of Fig. 2 in comparison with the ARM surface fluxes. As shown in the figure, the surface fluxes from ARM and LIS are close, except that they are different from days 4 to 9. Experiment L02 tests the sensitivity of clouds to surface fluxes from different data sources.

3. The 2000 case for springtime clouds

a. *Control experiment (C00)*

The control numerical experiment (C00) falls within the spring of 2000. Part of the large-scale forcing data

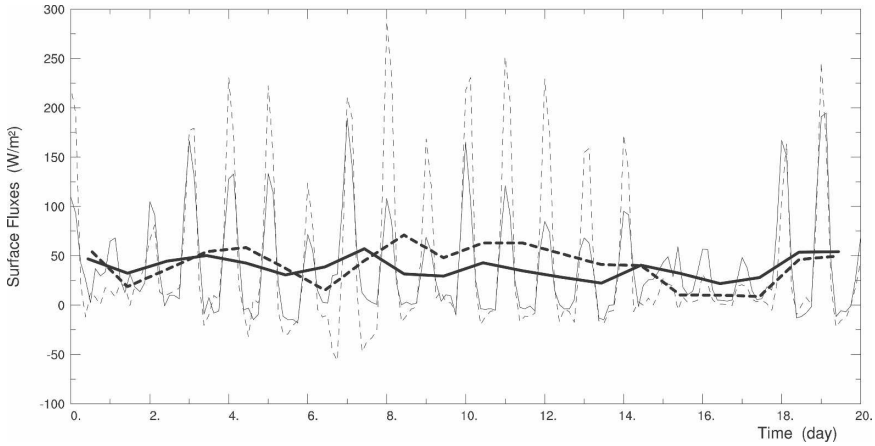

FIG. 1. Time series of surface fluxes for the 2000 case. The data start at 1730 UTC 1 Mar 2000. Solid and dashed lines denote latent and sensible heat fluxes, respectively. Thick lines display daily averaged values.

over the CART domain is displayed in Fig. 4, including large-scale horizontal temperature advection, horizontal advection of water vapor mixing ratio, and large-scale vertical velocity. The surface latent and sensible heat fluxes are also shown in Fig. 1. These forcing data start at 1730 UTC 1 March and end on 21 March 2000. Various synoptic systems pass through the domain in the following sequence: a synoptic cyclogenesis event (1–4 March), a cold front leg (5–8 March), an upper-level trough (9–11 March), nonprecipitating clouds (12–15 March), a cold front with frontogenesis (15–19 March), and stationary fronts (20–22 March).

The 3D GCE model is used to simulate the 20-day period. Modeled surface precipitation is compared with

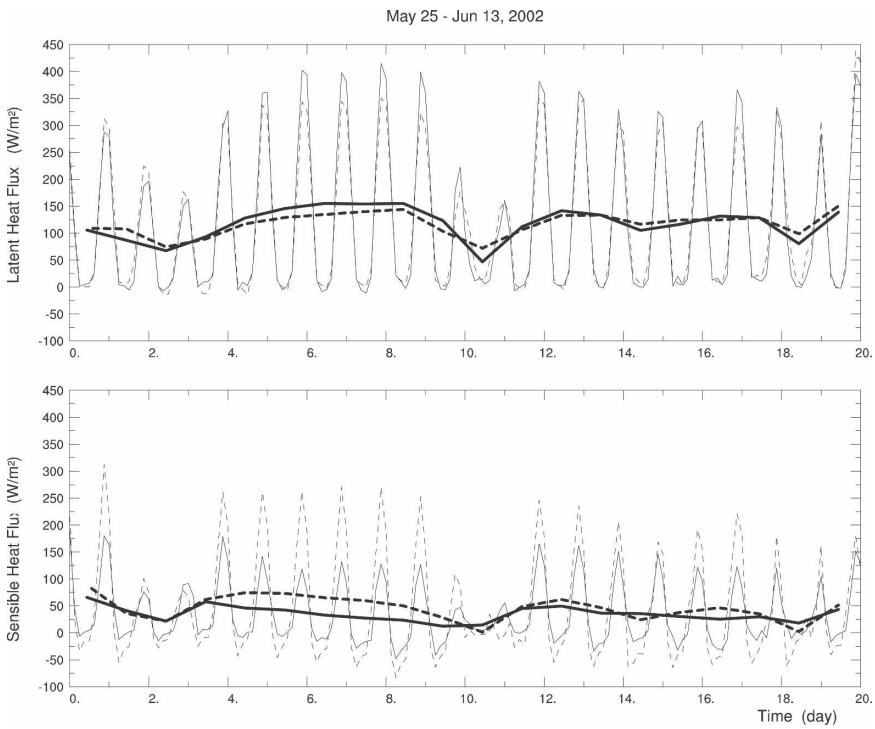

FIG. 2. Time series of surface fluxes for the 2002 case. All data start at 2030 UTC 25 May 2002. Solid and dashed thin lines represent the surface fluxes from the ARM observations and LIS land data assimilation system, respectively. Thick lines represent corresponding daily averaged values.

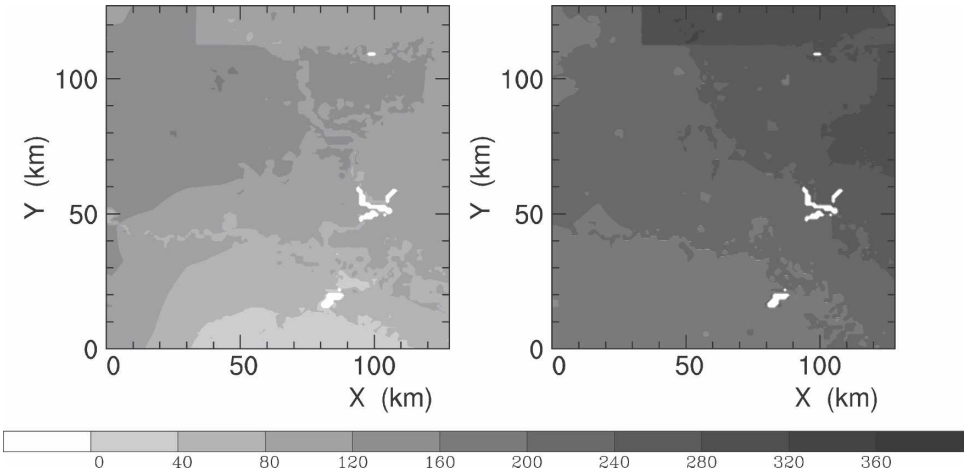

FIG. 3. Horizontal distributions of the LIS (left) sensible and (right) latent heat fluxes at day 1.

observations in Fig. 5 with thin and thick lines, respectively. In general, model surface precipitation agrees well with observations. Differences in intensity exist at days 6.5, 12.5, and 14.5. The accumulated surface precipitation amount is 6.3% smaller than was observed. Both modeled and observed surface precipitation rates have similar probability distribution functions (PDFs).

Time–pressure cross sections of retrieved liquid and ice water contents are displayed in Fig. 6. Since the retrievals have been well tested on thin nonprecipitating clouds but not on thick precipitating clouds (Dong and Mace 2003), shading density in the figure indicates the relative magnitude of the water contents. However, the edge of the shading shows clearly the extent of the clouds. Such distributions of water contents are used to evaluate the model results.

The domain-averaged water contents in the model are displayed in Fig. 7, where the liquid and ice water contents are defined as the total mixing ratios of liquid and ice water species, respectively. As shown in Figs. 6 and 7, the distribution of liquid water content in the model is similar to that retrieved. However, the distribution of model ice water content is quite different from the retrieved. Model ice water, in contrast to the retrieved, persists above 265 hPa as a residue of modeled clouds.

Modeled cloud fraction and relative humidity[1] with respect to water are compared with observations, respectively. Time–pressure cross sections of observed relative humidity and cloud fraction are shown in Fig. 8, and cross sections of the same variables from the model are shown in Fig. 9. A grid box in the model is defined as "cloudy" when the radar reflectivity $\mathrm{dB}Z_e \geq -35$, where the radar reflectivity is estimated from the mixing ratios of all water species using the algorithm of Luo et al. (2003). The distributions, as shown in Figs. 8 and 9, are similar for the main precipitation events such as those at day 1, 6.5, 9.5, and 15. However, the distribution of observed cloud fraction has many more fine structures than does the model. Modeled relative humidity, as shown in Figs. 8 and 9, is larger than was observed in the upper troposphere. The modeled relative humidity near 265 hPa increases gradually with time. It is around 50%–60%, implying that air there is close to saturation with respect to ice. The spuriously large relative humidity above 265 hPa is associated with excessive ice there.

Cloud fraction, temperature, and liquid and ice water contents from the model and observations are averaged over 20 days to show their mean profiles as a function of pressure (Fig. 10). Average liquid and ice water contents in the model are smaller and larger than those retrieved, respectively, although the difference between observations and the model is partly due to the way in which the values were obtained. This comparison indicates that excessive liquid water is converted to ice.

Cloud amount in the model, as shown in Fig. 10, is larger than observed. The modeled cloud amount is ~20% more than was observed from 800 to 250 hPa. The model air temperatures are 7.8 K lower and 3.5 K higher than observations at 100 and 265 hPa, respectively. The simulated near-surface air temperature is 5 K higher than the observations. The temperature differences between the model and observations are due not only to the specified large-scale forcing errors but also the overprediction of cloud residues in the upper

[1] Relative humidity is defined over water except when specified in the paper.

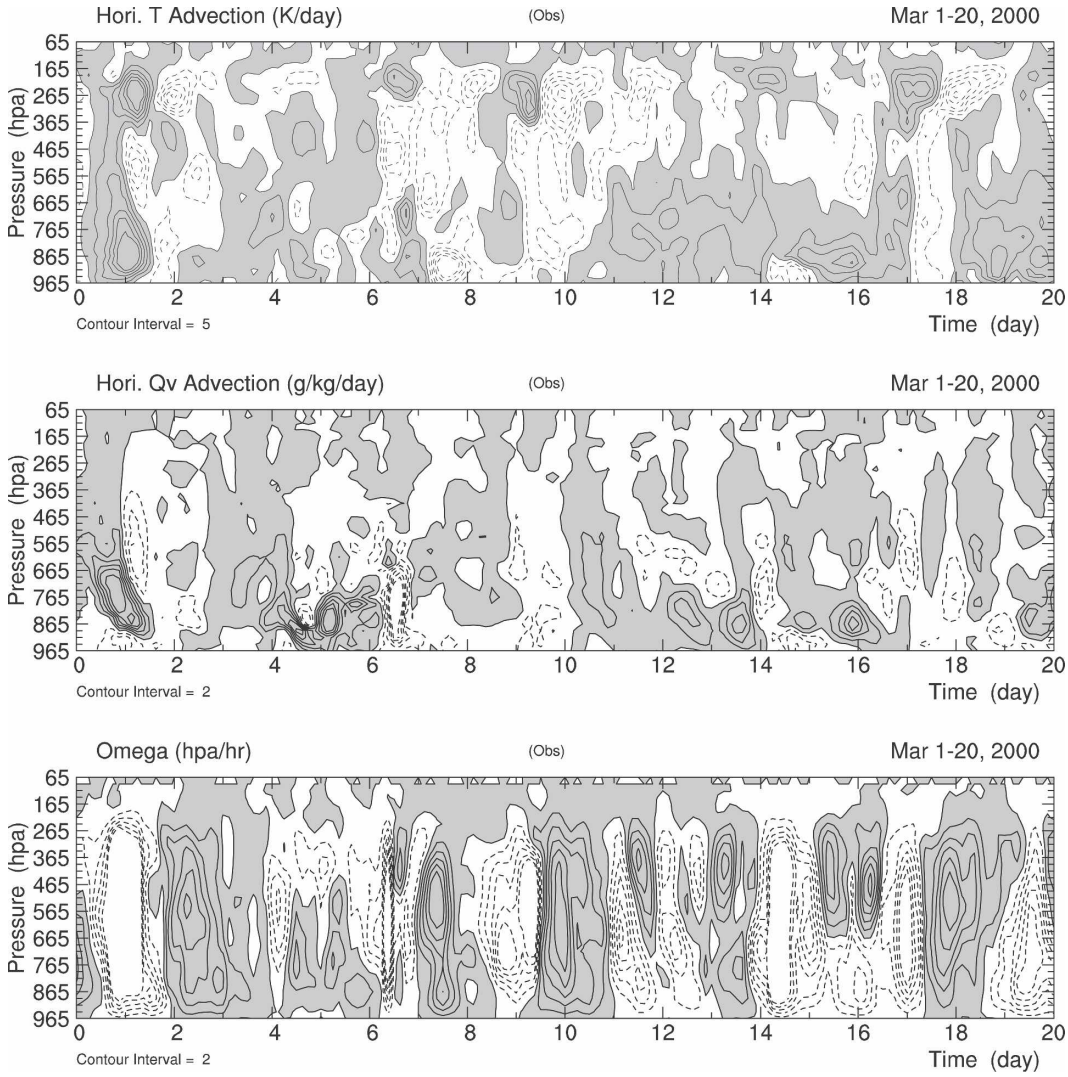

FIG. 4. Time–pressure cross sections of (top) large-scale horizontal temperature advection, (middle) horizontal advection of water vapor mixing ratio, and (bottom) large-scale vertical velocity. Data start at 1730 UTC 1 Mar 2000. Shaded areas indicate positive values; dashed and solid lines represent negative and positive valued contour levels, respectively.

troposphere. Since cloud ice in the upper troposphere emits longwave radiation into space and absorbs upward longwave radiation from the air and land surface below, excessive cloud ice near 165 hPa decreases the temperature at ~100 hPa and increases the temperature at ~265 hPa. Meanwhile, excessive cloud ice in the upper troposphere also increases the downward longwave radiation, which in turn contributes partly to the overprediction of air temperature near the surface.

Figure 11 displays the 20-day average profiles of water vapor mixing ratio and relative humidity against pressure. The difference in the mixing ratios between the model and observations decreases from 1.1 g kg^{-1} near the surface to zero at the tropopause. In contrast, the difference in relative humidity generally increases with height, from nearly zero at the surface to 30% at 265 hPa. The spuriously high relative humidity in the upper troposphere is associated with the overprediction of cloud ice in the upper troposphere, since cloud ice increases (or decreases) through deposition (or sublimation) when air is saturated (or unsaturated) with respect to ice.

b. Dimensionality experiments

In contrast to C00, 2D CRM simulations are analyzed for the sensitivity of clouds to dimensionality in this subsection. For a better understanding, the difference in physics between 2D and 3D CRMs is discussed

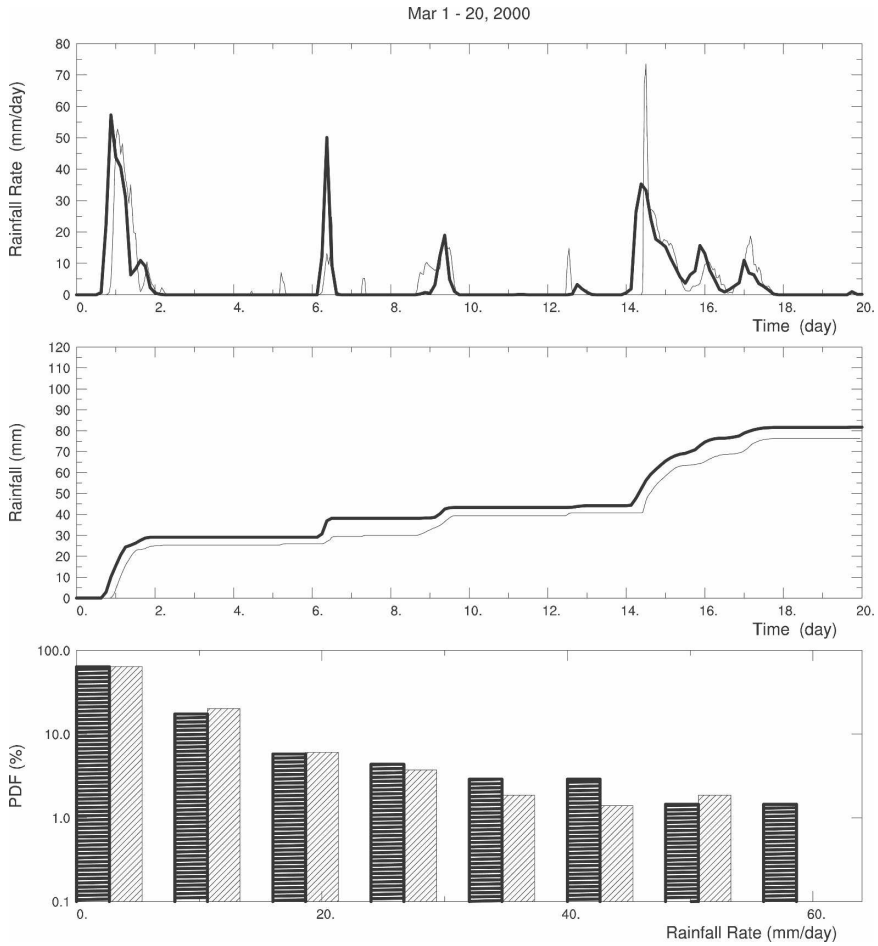

FIG. 5. Surface precipitation for the spring 2000 period. Thick and thin lines represent the observations and control experiment C00, respectively. (top) Surface precipitation rate and (middle) accumulated rainfall. (bottom) The PDF of surface precipitation.

first. Buoyancy damping is a physical concept of an atmospheric system whose length scale is smaller than the Rossby radius of deformation. The concept was discussed in previous studies for specific applications (Bretherton and Smolarkiewicz 1989; Mapes 1993; Nilsson and Emanuel 1999; Sobel and Bretherton 2000; Raymond and Zeng 2000). With an analytical model for a dry stratified atmosphere, the appendix shows the relative importance of gravity waves and friction in buoyancy damping and exhibits the sensitivity of buoyancy damping to dimensionality. Buoyancy damping in a 3D dry model, as shown in the appendix, consists of two stages. In the first stage, an initial temperature perturbation (or buoyancy) propagates outward due to gravity waves, resulting in the decrease of the temperature perturbation with time since the perturbation is distributed into a wider area. In the second stage, the perturbation dissipates due to friction in the wider area. Thus, when friction is small, the perturbation damps mainly in the first stage, implying that 3D buoyancy damping is insensitive to friction. In contrast, the buoyancy in a 2D model damps only due to friction. Consequently, 2D buoyancy damping is sensitive to friction. Therefore, the difference in sensitivity of buoyancy damping to friction between 2D and 3D models implies the sensitivity of buoyancy damping to dimensionality.

Based on the sensitivity of buoyancy damping to dimensionality, it is inferred that clouds are sensitive to model dynamic structure through cloud microphysics parameterization. Consider an isolated temperature perturbation that is generated as a result of a convective cloud. The perturbation damps with time in a 3D CRM even when model friction (e.g., spatial smoothers) is weak. In contrast, a similar perturbation does not obviously damp in a 2D CRM when model friction is weak, resulting in many vertical oscillations that travel horizontally as gravity waves.

Consider a 2D CRM with many vertical oscillations.

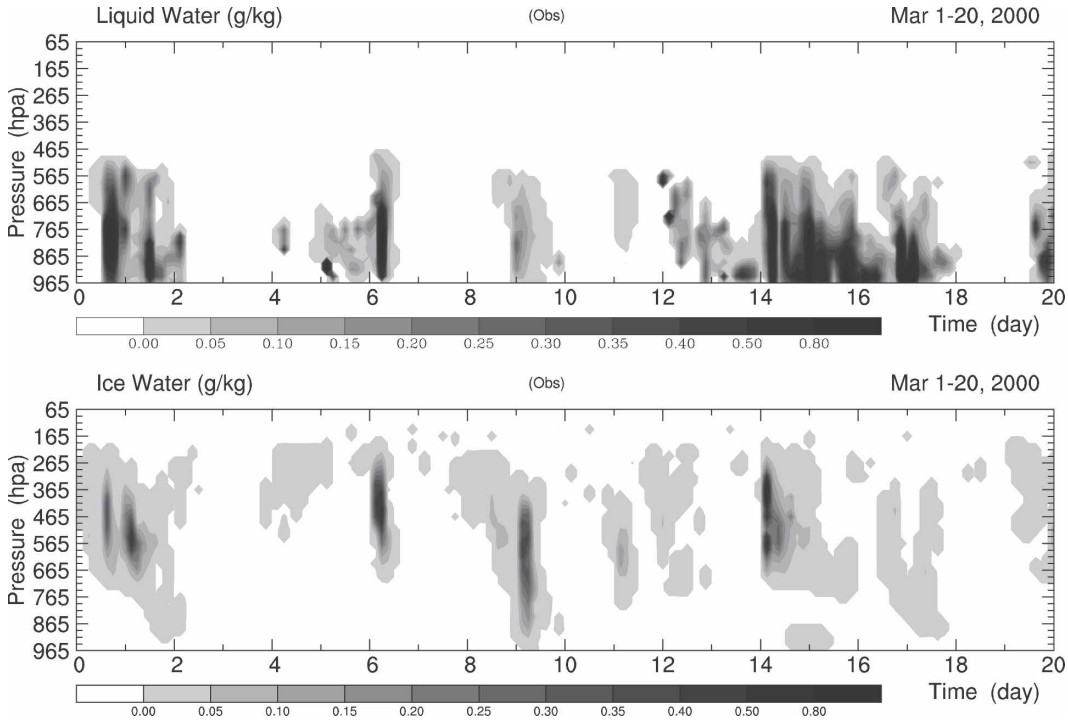

FIG. 6. Time–pressure cross sections of retrieved liquid and ice water contents starting from 1730 UTC 1 Mar 2000.

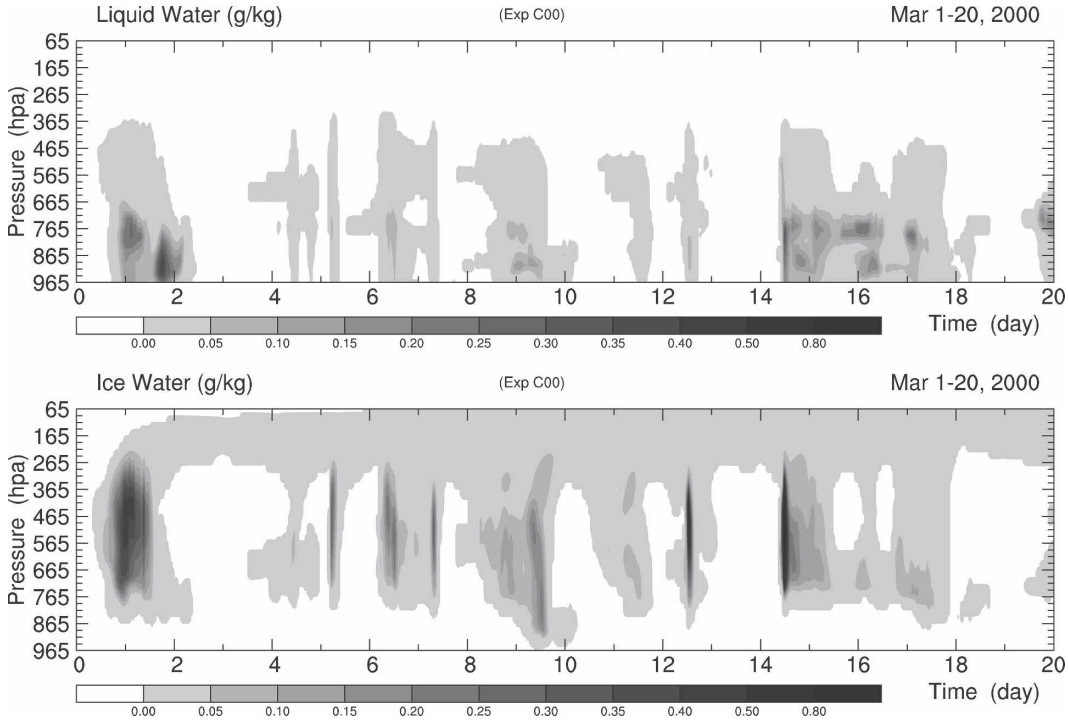

FIG. 7. Time–pressure cross sections of (top) liquid and (bottom) ice water contents obtained from the control experiment C00 for the spring 2000 period.

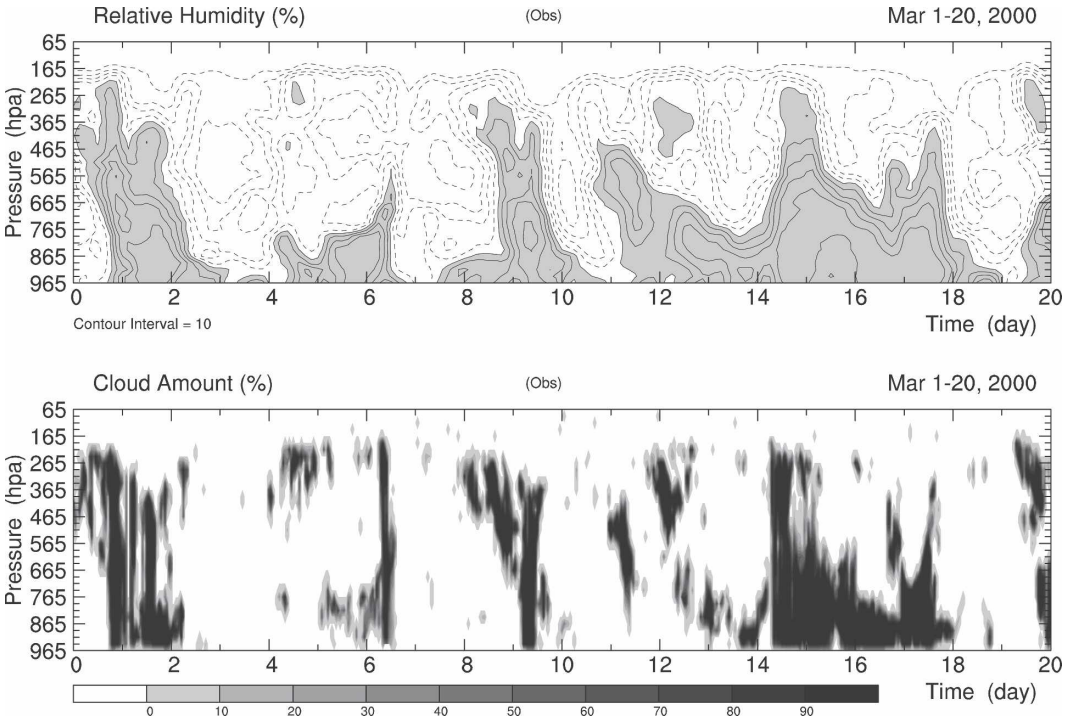

FIG. 8. Time–pressure cross sections of observed (top) relative humidity and (bottom) cloud fraction starting from 1730 UTC 1 Mar 2000. Shaded areas in top panel indicate a relative humidity of more than 50%; dashed and solid lines represent the contour levels with relative humidity smaller and larger than 50%, respectively.

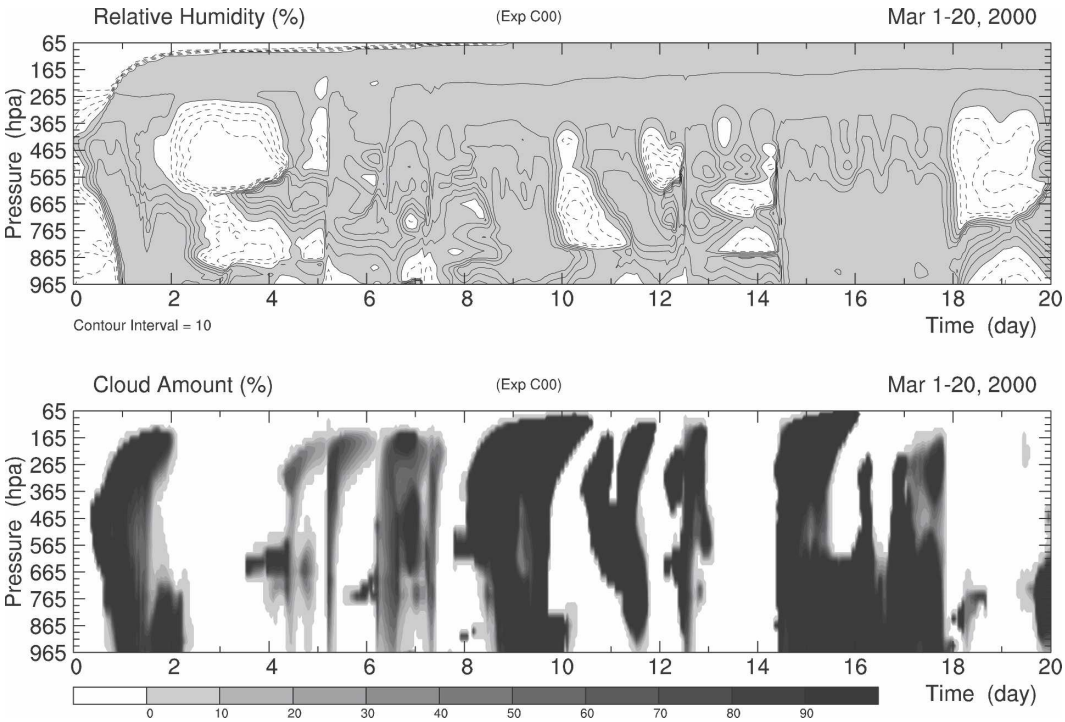

FIG. 9. Same as in Fig. 8, but for relative humidity and cloud fraction from the control experiment C00 for the spring 2000 period.

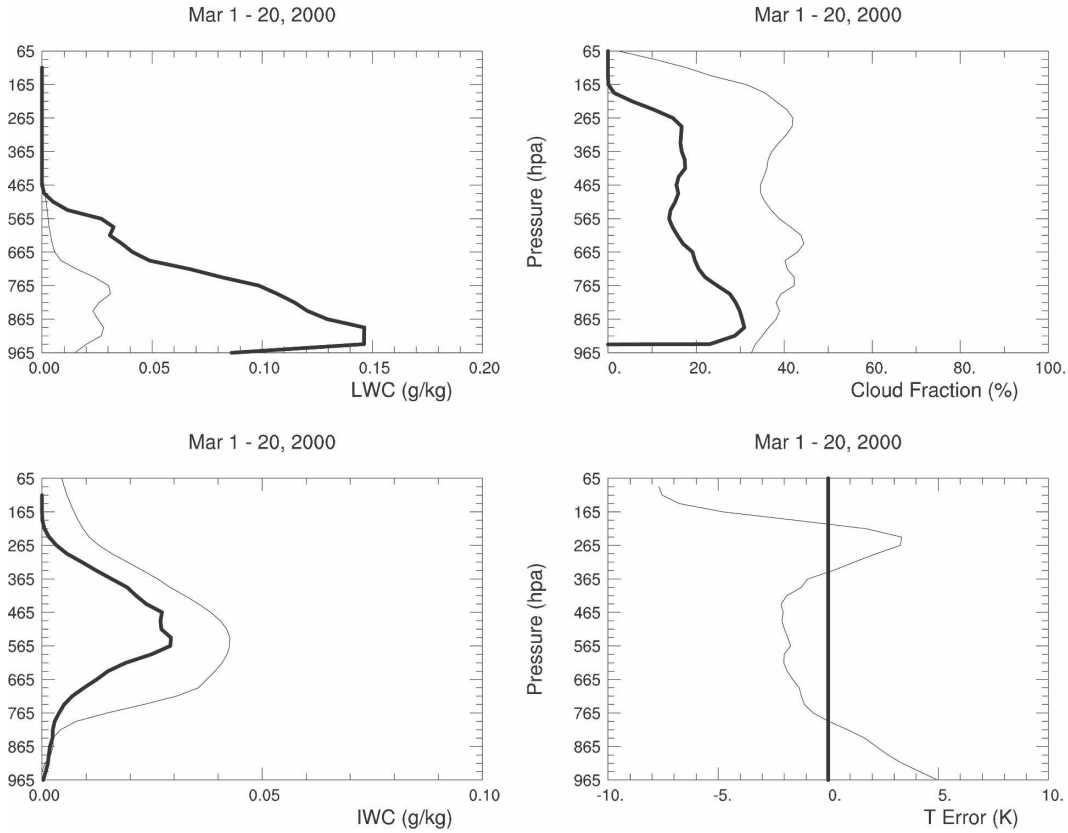

FIG. 10. Twenty-day mean profiles of (top left) liquid and (bottom left) ice water content, (top right) cloud fraction, and (bottom right) air temperature difference between the model and observations against pressure in the 2000 case. Thick and thin lines represent variables from observations and experiment C00, respectively.

Since precipitation is tightly related to vertical velocity, it is expected that precipitation would fluctuate rapidly in a 2D CRM. If the conversion rate from ice to snow is large, little cloud ice is expected in the upper troposphere because of the vertical oscillations (see section 5b for details). However, vertical oscillations can be controlled by spatial smoothers. When spatial smoothers are strong, buoyancy damps due to friction and vertical oscillations are weak. As a result, cloud ice cannot be converted to snow efficiently, and thus ice persists as a cloud residue in the upper troposphere.

The preceding analysis is tested with four 2D experiments that are listed in Table 2. The first one, D00a, adopts the same parameters as the 3D experiment, C00, except for 512 × 41 grid points. Its pressure–time distribution of cloud ice is similar to C00, showing much

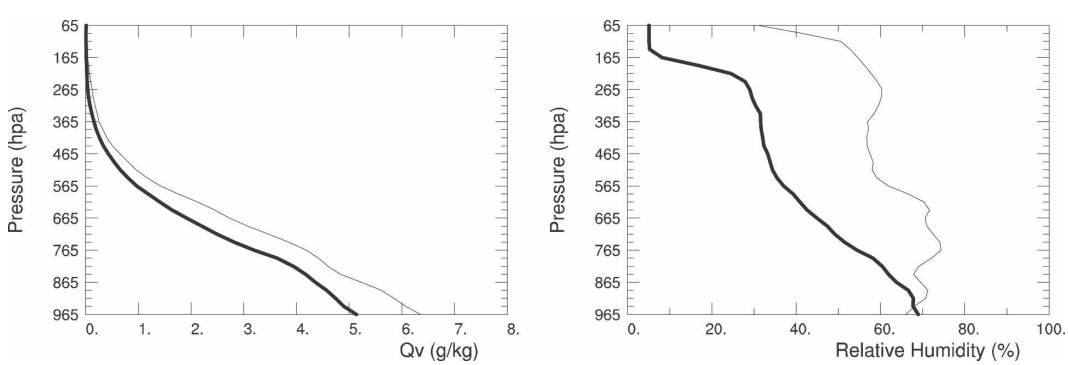

FIG. 11. Same as in Fig. 10, but for relative humidity and the mixing ratio of water vapor.

TABLE 2. List of 2D numerical experiments.

Experiment name	Grid point	Comments
D00a	512 × 41	Control run; 2D version of C00
D00b	512 × 41	D00a but weak spatial smoother
D00c (or D00)	512 × 41	D00b but stronger conversion of cloud ice to snow
D00d	128 × 41	D00c but small domain size

cloud ice in the upper troposphere although the cloud ice content is reduced. The second 2D experiment, D00b, is similar except for a weak spatial smoother. Using 42.5 m for the mixing length for subgrid turbulence instead of the 250 m in C00, the experiment results in less cloud ice in the upper troposphere than D00a, supporting the conclusion that spatial smoothers can influence cloud ice in the upper troposphere.

The third 2D experiment D00c, also referred to here as experiment D00, still uses 42.5 m as the mixing length for subgrid turbulence. However, it increases the conversion of cloud ice to snow by changing the related terms in the scheme of Lin et al. (1983) to those in the scheme of Rutledge and Hobbs (1984). Since D00 has the least cloud ice in the upper troposphere of all three 2D experiments, it is analyzed next in detail in comparison with the 3D experiment C00.

The surface precipitation from D00 (Fig. 12) shows rapid fluctuations at days 6.5, 14.5, and 17 in contrast to observations and the 3D model. However, after being averaged over a long period, the surface precipitation rate and its accumulated amount are close to the ob-

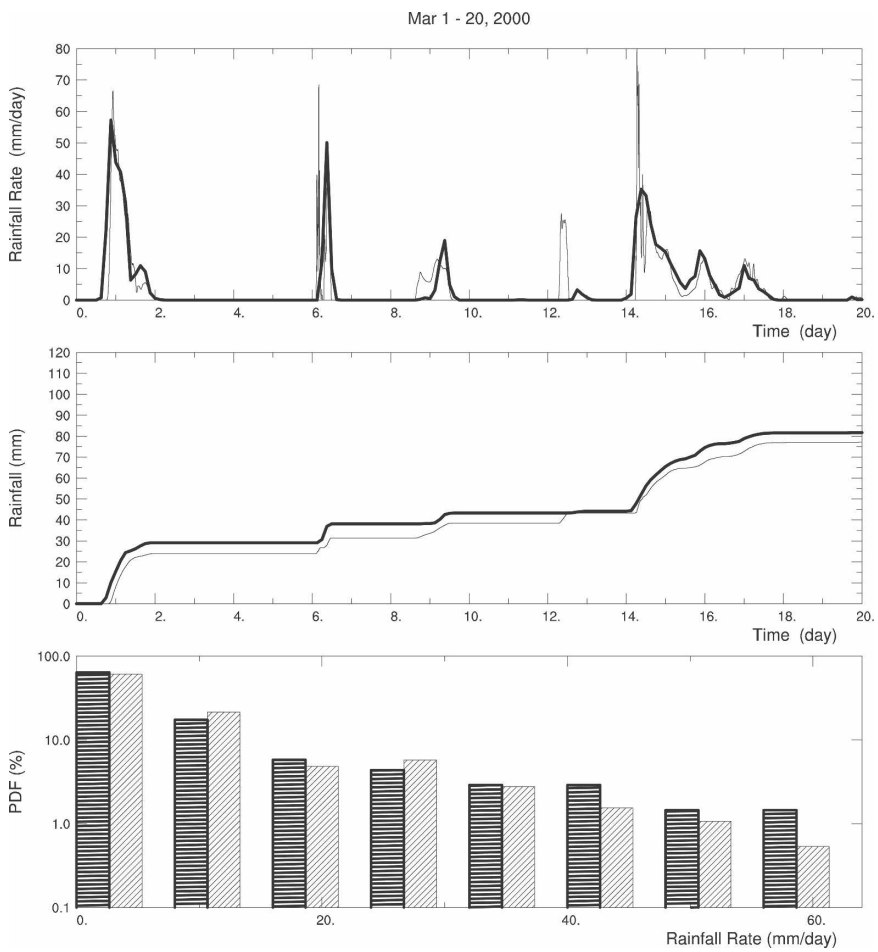

FIG. 12. Same as in Fig. 5, but for the experiment D00 (a 2D numerical experiment for the 2000 case).

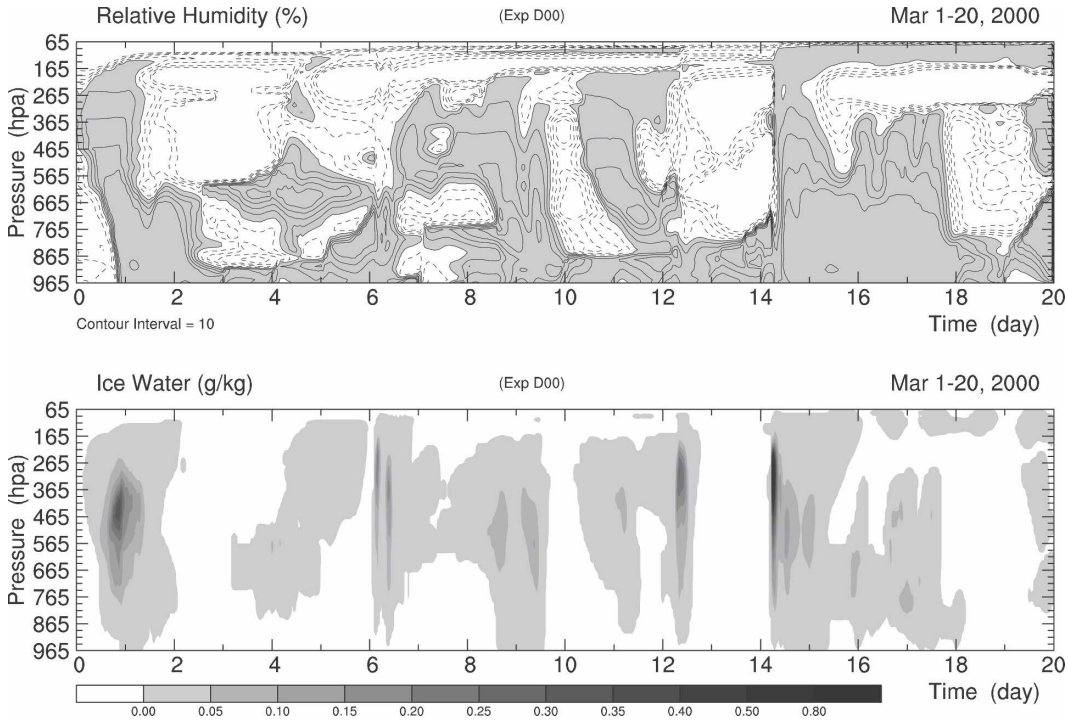

FIG. 13. Time–pressure cross sections of (top) relative humidity and (bottom) ice water content in experiment D00 (a 2D numerical experiment for the 2000 case).

servations. The final accumulated precipitation amount after the 20-day integration is 5.6% smaller than that observed. This 5.6% difference is slightly smaller than the corresponding difference of 6.3% for the 3D model, indicating that more water aloft is converted to precipitation in the 2D model than in the 3D one.

Time–pressure cross sections of relative humidity and ice water content for D00 are displayed in Fig. 13. When compared with Figs. 8 and 9, the figure shows that the relative humidity in the upper troposphere changes irregularly, differing from the observations or the 3D model significantly. In addition, the distribution of ice water in the model is different from that retrieved. It is also different from the 3D model by having periods without cloud ice in the upper troposphere. Another 2D experiment, D00d, with 128×41 grid points shows the sensitivity of cloud properties to domain size in 2D. The modeled surface precipitation is similar to that in Fig. 12 except for stronger surface precipitation fluctuations. The modeled clouds have distributions similar to those in Fig. 13 except for many fine structures in the middle troposphere. The fine structures associated with relative humidity and cloud ice in the middle troposphere correspond to the rapid fluctuation in modeled surface precipitation. The 2D simulations, in contrast to the 3D, show that fluctuations in surface precipitation are sensitive to domain size.

Figure 14 displays time-average values of relative humidity, cloud fraction, and the horizontal variance of temperature against pressure for experiments C00 and D00 as well as the observations. The figure shows that the temperature variance is generally larger in the 2D experiment than in the 3D one, especially in the upper and the lower troposphere. Since the temperature variance measures approximately the average height deviation of air parcels from their original places, its contrast between the 2D and 3D experiments implies that local circulations are stretched vertically longer in the 2D experiment than in the 3D one, and therefore it is reasoned that more cloud water and ice are converted to precipitating water in the 2D experiment than in the 3D one.

Figure 14 also shows that relative humidity is closer to observations on average in the 2D experiment than in the 3D one, and cloud fraction is smaller in the 2D experiment than in the 3D one although cloud fractions in both experiments are larger than the observations. Such differences between the 2D and 3D modeled precipitation and clouds support the theoretical analysis of clouds to dimensionality.

c. *Other sensitivity experiments*

The 3D experiment, C00, shows excessive clouds in the model. Just as was shown in the preceding subsec-

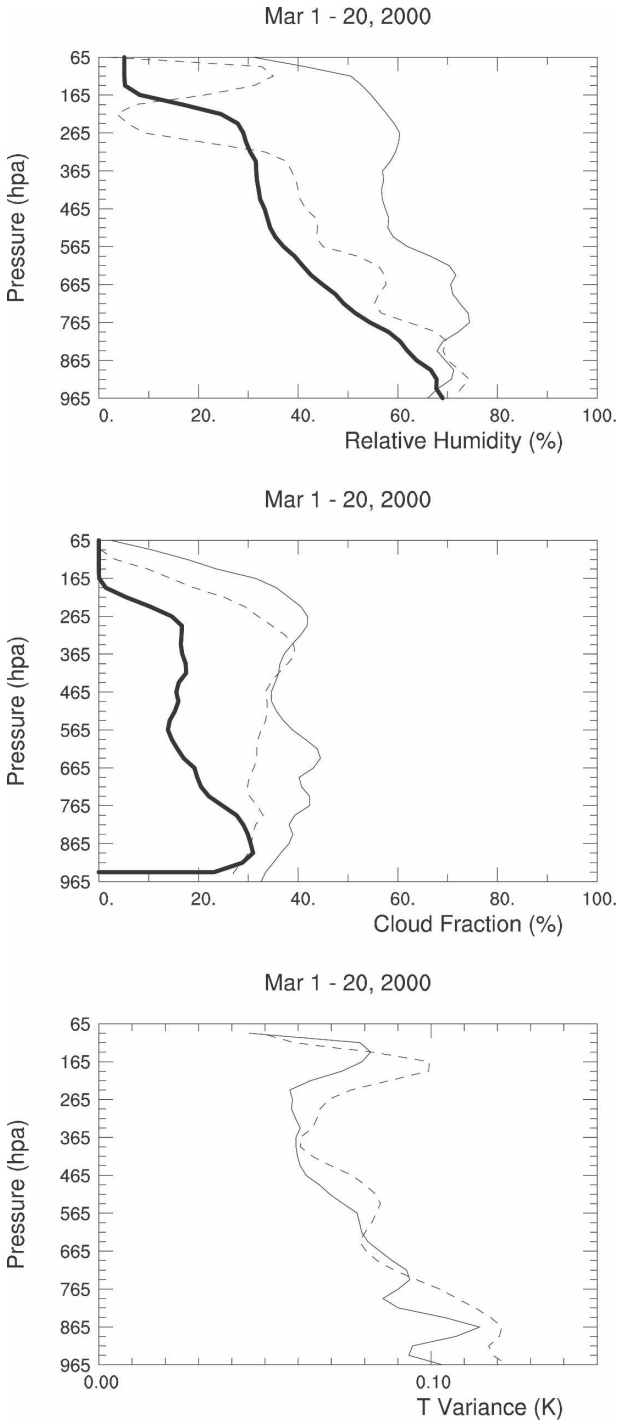

FIG. 14. Twenty-day mean profiles of (top) relative humidity, (middle) cloud fraction, and (bottom) temperature variance against pressure in the 2000 case. Thick lines represent observed variables; thin lines represent variables from experiment C00; and thin dashed lines represent variables from experiment D00.

tion, the 2D model structure reduces the excessive clouds. Even so, comparing 2D simulations versus observations is not encouraged for model parameterization tuning since the 2D structure is an artificial factor. In this subsection, additional sensitivity experiments are done to test the sensitivity of clouds to other atmospheric factors.

In contrast to C00, two experiments with $256 \times 256 \times 41$ grid points are done with the horizontal resolutions of 1 and 2 km, respectively. Their results, although differing in details, still exhibit cloud overprediction in the upper troposphere, showing that domain size is not a factor for the cloud overprediction.

An experiment with the sedimentation of cloud ice is done since the sedimentation can be an important process (e.g., Wu et al. 1999; Hong et al. 2004). After introducing the sedimentation of cloud ice (Starr and Cox 1985), model cloud residues are improved. The difference between the model and observations in terms of relative humidity, in contrast to Fig. 9, increases *slowly* with time near 165 hPa. The distribution of cloud ice in the upper troposphere contains breaks in a time–pressure cross section. Obviously, the cloud simulation is improved when cloud ice sedimentation is taken into account. Even so, the modeled relative humidity and cloud ice are still higher than was observed.

4. The 2002 case for summertime clouds

a. Control experiment (C02)

In contrast to the springtime case in the preceding section, a summertime case is studied in this section. Figure 2 displays the ARM surface latent and sensible heat fluxes versus time. Figure 15 displays some of the large-scale forcing data for the 2002 case, namely, large-scale horizontal temperature advection, horizontal advection of water vapor mixing ratio, and large-scale vertical velocity. All data start at 2030 UTC 25 May 2002 and last for 20 days. Compared with Fig. 4, Fig. 15 shows that the 2002 case has weaker large-scale forcing (e.g., large-scale vertical velocity in the planetary boundary layer). Figures 1 and 2 show that the 2002 case has strong surface latent heat flux both in amplitude and daily average.

The control experiment for the 2002 case (C02) is a 20-day simulation with the same parameters as C00. Figure 16 displays the observed and modeled surface precipitation versus time. The strong precipitation events are fairly well captured. Just like in the other CRMs (Xu et al. 2002), the precipitation events at days 1.5 and 17 are delayed. To test the reason for the delay in precipitation, a numerical experiment was made that

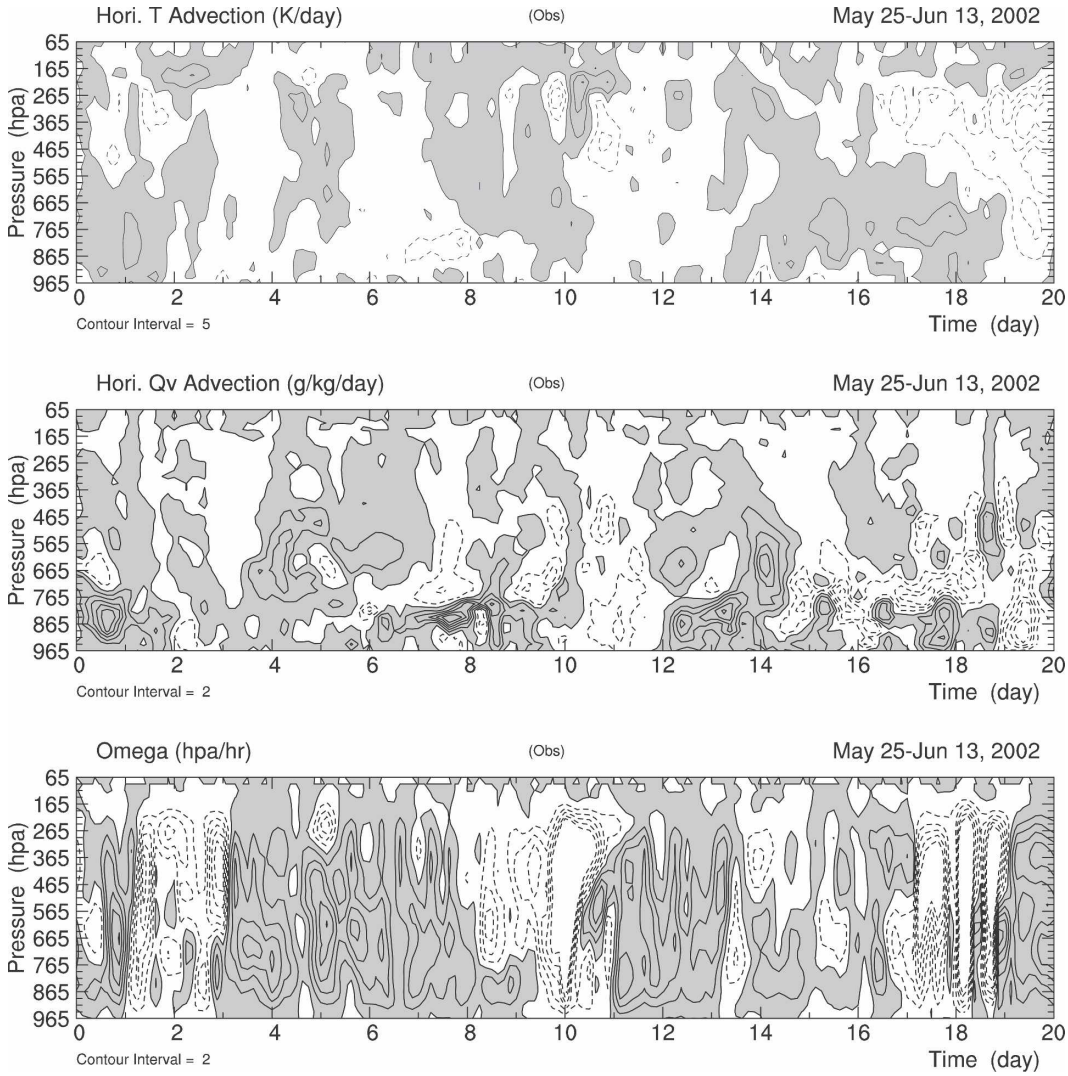

FIG. 15. Same as in Fig. 4, but for the 2002 case. Data start at 2030 UTC 25 May 2002.

started at day 1 with an artificial increase in water vapor in the planetary boundary layer. The results (figure omitted) show that the three precipitation events from days 1–3 are modeled well and the accumulated precipitation amount also agrees well with observations. This infers that the delay in precipitation on day 1.5 in C02 can be attributed to the lack of proper triggers for convective clouds.

Two spurious precipitation events, as shown in Fig. 16, appear at days 13.5 and 14.2 in contrast to observations. The precipitation event at day 14.2 is initiated by large convective available potential energy (CAPE; which is directly proportional to surface relative humidity when the air surface temperature is given) that is reasoned from Fig. 17, and the event is further intensified by the upward large-scale motion in the middle troposphere (see Fig. 15). To test the influence of previous accumulative errors on the spurious precipitation events, a new simulation was done that started at day 13. In this experiment (figure omitted), the precipitation event at day 13.5 disappears, and the precipitation event at day 14.2 is significantly weakened but still there. In summary, experiment C02 and the other two experiments show that convective initiation, water spinup, and large-scale forcing influence the simulation of summertime precipitation.

Figure 16 also shows that the accumulated precipitation amount in the model is smaller than the observations by 10.2%. Also, the PDF for the modeled precipitation rate is similar to observations at small rainfall

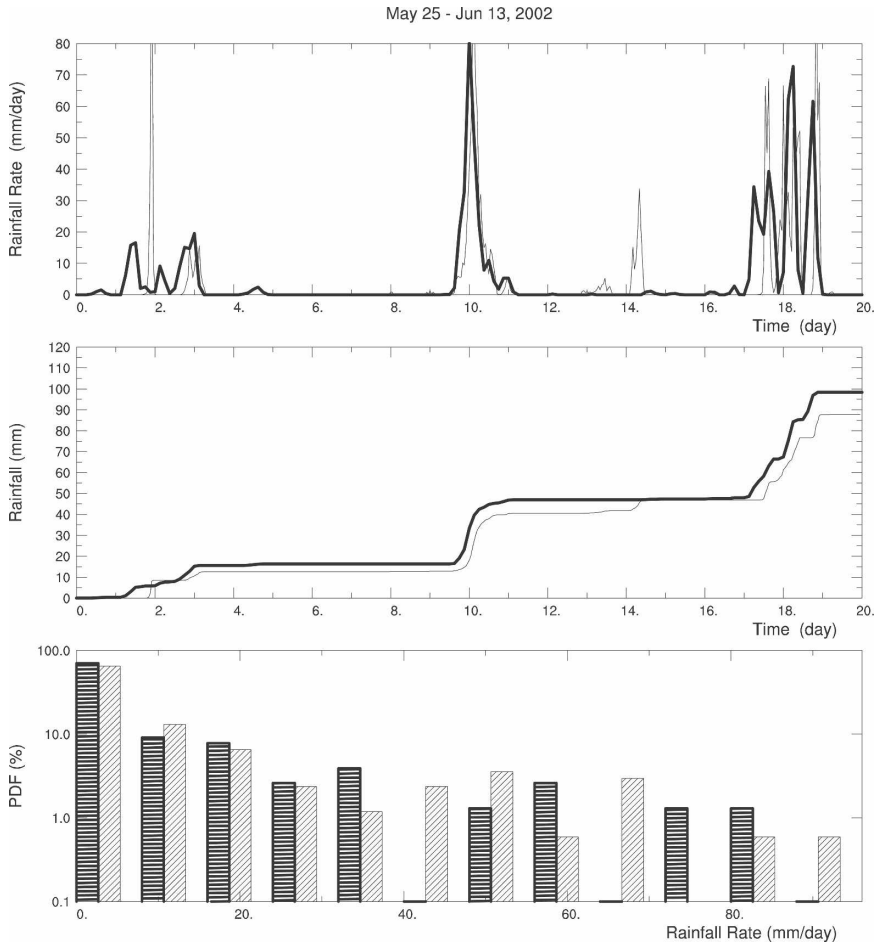

FIG. 16. Same as in Fig. 5, but for the 2002 case. The numerical experiment is C02.

rates but different at high rainfall rates. In general, the model has a reasonable accumulated precipitation and rainfall rate PDF compared to observations.

Figure 17 displays time–pressure cross sections of observed relative humidity and cloud fraction, showing the diurnal variation of relative humidity and cloud amount in the lower troposphere. Figure 18 displays the same variables from the model. As shown in these two figures, the model relative humidity is larger than observations, especially in the upper troposphere. A pronounced diurnal variation of low clouds exists in the model more so than in the observations.

Twenty-day average values of water vapor mixing ratio and relative humidity (Fig. 19) show that the observations and model are similar in terms of water vapor mixing ratio but different for relative humidity. The modeled relative humidity is ~30% higher than observed in the upper troposphere. Compared with Fig. 11, it shows that the differences between the model and observations for humidity are similar in both the 2000 and 2002 cases, although the surface water vapor mixing ratio and latent heat flux are much larger for the 2002 case.

b. *Land surface flux experiment (L02)*

Surface fluxes are necessary in an MMF to help drive large-scale circulations over continents. Unlike the numerical experiments in the preceding sections, no observational fluxes are available in an MMF. Thus, it is of interest to test the sensitivity of cloud properties to surface fluxes when the surface fluxes are provided from a land surface model. This section describes such a sensitivity experiment and its impact on the simulation of clouds and precipitation.

Experiment L02 follows control experiment C02 except that surface fluxes as well as land surface temperature come from LIS. The LIS data are obtained after a 15-yr spinup driven by observational data with a 1-km horizontal resolution (see section 2a for details). Figure 2 displays the domain-average values of the surface fluxes. The LIS fluxes have a strong diurnal signature very similar to the ARM data. The 20-day average val-

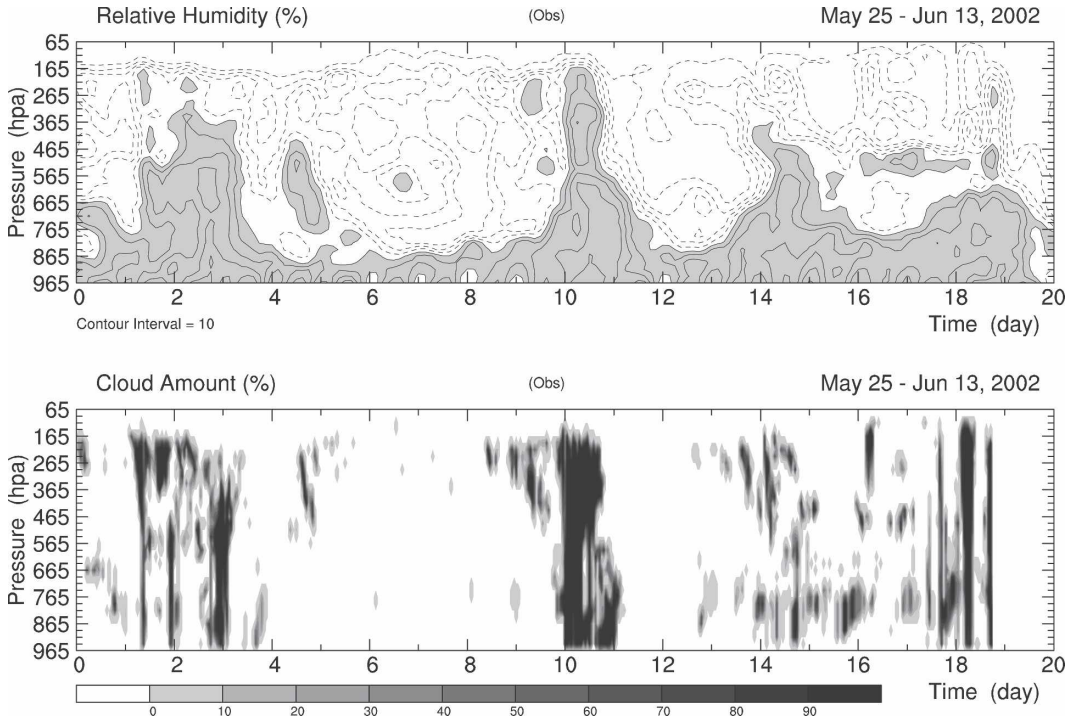

FIG. 17. Same as in Fig. 8, but for the 2002 case.

ues of latent and sensible heat fluxes from LIS are 117.1 and 44.3 W m^{-2}, while the corresponding ARM data are 117.4 and 34.9 W m^{-2}, respectively. However, the LIS sensible heat fluxes from days 4 to 9 are larger than the ARM values in both amplitude and daily average.

In experiment L02, LIS fluxes are assumed to be horizontally uniform. Surface precipitation characteristics (Fig. 20) are very similar to those in C02, but the rain-rate PDF between the model and observations is different at high rainfall rates. Time–pressure cross sections of relative humidity and cloud amount from L02 are shown in Fig. 21. This and other figures on water content (figure omitted) indicate that cloud residues are still overpredicted in the upper troposphere. However, the diurnal variation of cloud amount in the lower troposphere from days 4 to 9 is superior to C02. This improvement is attributed to the large LIS sensible and small latent heat fluxes from days 4 to 9 (see Fig. 2 for details). When the sensible heat flux increases and the latent heat flux decreases, the surface relative humidity decreases. As a result, the lifting condensation level increases, and in turn cloud amount in the lower troposphere decreases. This connection between surface fluxes and the diurnal variation of clouds in the lower troposphere (as shown in Figs. 18 and 21) is consistent with the difference in relative humidity in the planetary boundary layer between the two experiments.

The ARM and LIS fluxes come from different sources. The ARM surface fluxes used in the control experiment come from the EBBR stations, which use the Bowen ratio to partition the fluxes. There are a total of 14 EBBR stations. A grid of 0.5 × 0.5 degrees was first set up to cover the ARM SCM (single-column model) domain. Next, the Barnes scheme with a length scale of 80 km was used to fill all the boxes. These 0.5 × 0.5 degree boxes within the SCM domain were then averaged to get the area-averaged surface fluxes. Based on this procedure for the ARM surface flux data, it is inferred that some uncertainty is introduced into the ARM-averaged fluxes due to the small representative scale of land variables. In contrast, the LIS fluxes were obtained from a land surface model that was driven with observational data of 1-km resolution (see section 2a for details). Although the LIS fluxes at a point are not as accurate as the ARM fluxes, their fine resolution may lead to better area-averaged fluxes than those from "sparse" observational stations. However, this topic remains open and further comparisons between the two kinds of surface flux data are needed.

5. Discussion

a. Clouds and large-scale circulations

Current MMFs produce "Red Spots" (or excessive precipitation) in the Tropics and overactive Madden–

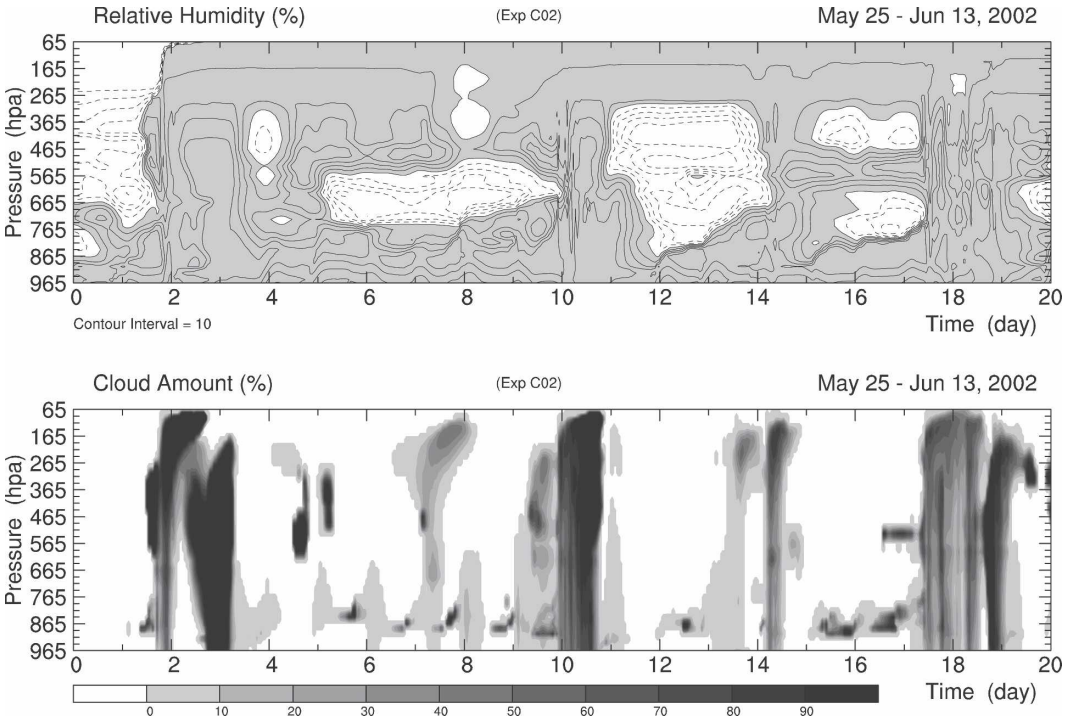

FIG. 18. Same as in Fig. 9, but for the 2002 case. Data are from the control experiment C02.

Julian oscillations (e.g., Khairoutdinov and Randall 2001; Khairoutdinov et al. 2005; Chern et al. 2005, unpublished manuscript). Such biases could be due to the excessive clouds in CRMs, because clouds can interact with radiation to form a positive feedback between the large-scale circulation and cloud activity.

The interaction between clouds and large-scale circulations is understandable. Thermodynamics dominate atmospheric circulations on sufficiently large scales (Neelin and Held 1987; Emanuel 1995, 1999; Raymond 1995, 2000; Raymond and Zeng 2000; Zeng et al. 2005). Thus, large-scale vertical circulations are sensitive to atmospheric radiative cooling rate and the surface fluxes from the underlying surface (e.g., Zeng et al. 2005). On one side, clouds modulate radiation greatly (e.g., Albrecht and Cox 1975) that in turn change large-scale circulations. On the other side, large-scale circulations modulate clouds and precipitation (e.g., Raymond and Zeng 2005). Thus, there is a positive feedback between clouds and radiation (e.g., Raymond and Zeng 2000). The positive feedback suggests that accurate simulation of tropical precipitation requires the proper simulation of clouds. In response to this reasoning, two 20-day, continental periods are simulated in the present paper for the evaluation of clouds and surface fluxes in CRMs.

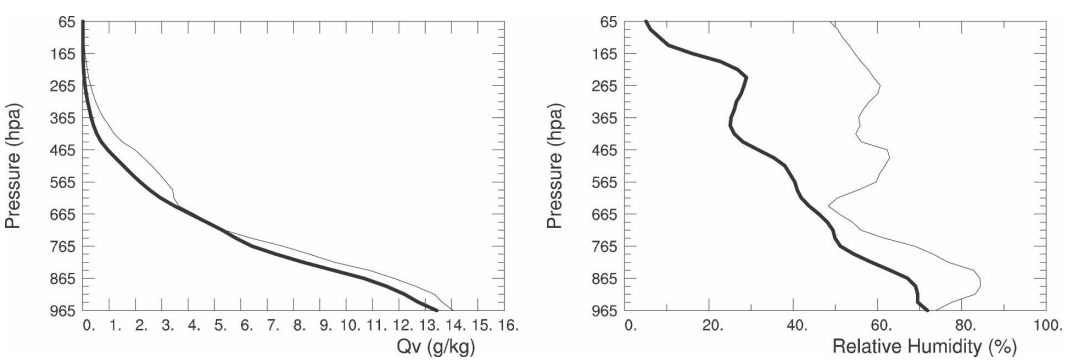

FIG. 19. Same as in Fig. 11, but for the 2002 case. The numerical experiment is C02.

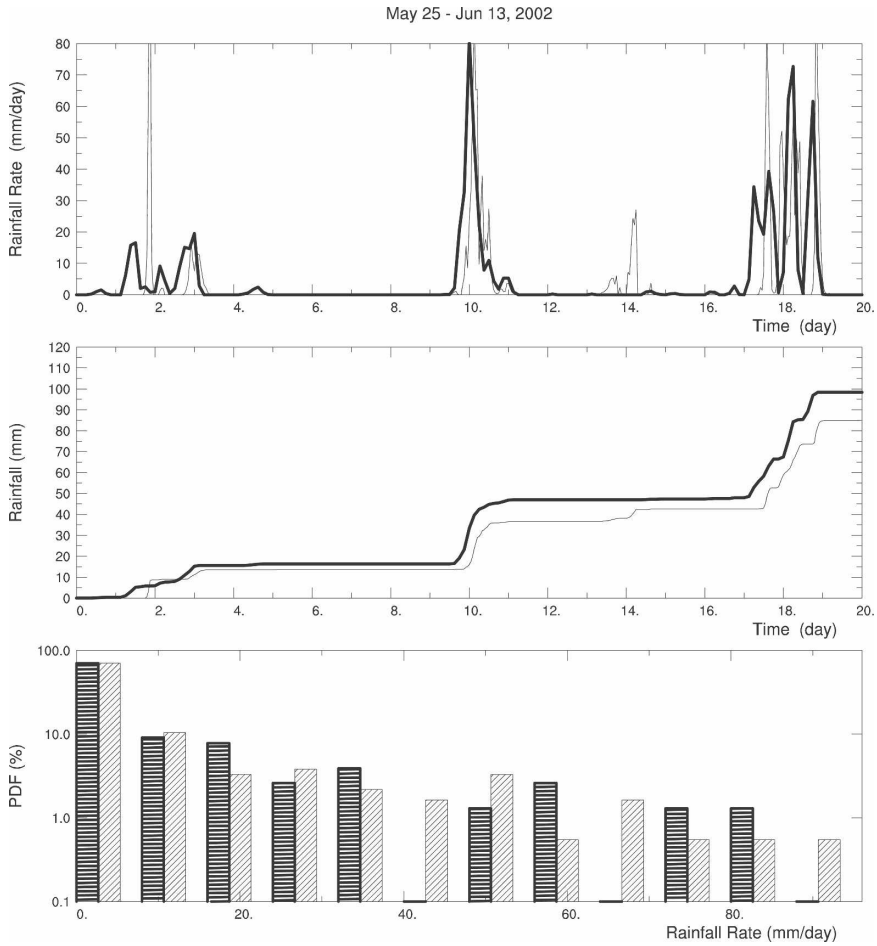

FIG. 20. Same as in Fig. 16, but for the 2002 case and experiment L02.

b. Buoyancy damping and cloud simulations

Because of available computational sources, current MMFs usually employ 2D CRMs to represent clouds. However, previous studies presented differing conclusions on the sensitivity of cloud properties to dimensionality (see section 1c for details). In the present paper, the difference in physics between 2D and 3D CRMs is studied with numerical simulations as well as observations and theoretical analysis, providing an explanation for the conflicting results.

Differences between the 2D and 3D simulations are attributed to the energy transfer between scales (e.g., Lilly 1969; Moeng et al. 1996) and buoyancy damping, where the latter is important near the tropopause because the energy transfer is associated with nonlinear momentum terms (e.g., Lesieur 1990) and the nonlinear terms due to convective cells are not important there.

With an analytical model, the appendix shows that buoyancy damping differs in 2D and 3D dry models. In a 3D dry model, buoyancy damping consists of two stages. An initial temperature perturbation (or buoyancy) first propagates outward due to gravity waves, resulting in the decrease of the temperature perturbation with time since the perturbation is distributed into a wider area. Then, the perturbation dissipates due to friction in the wider area. When friction is small, the perturbation damps mainly on the first stage, implying that 3D buoyancy damping is insensitive to friction. In contrast, the perturbation in a 2D model with no friction does not damp, resulting in vertical oscillations that travel horizontally as gravity waves. Therefore, buoyancy damps only because of friction in a 2D model, making 2D buoyancy damping sensitive to friction.

In CRMs, convective clouds generate isolated temperature perturbations. Just as shown in the appendix, the temperature perturbations damp rapidly in 3D models. However, the corresponding perturbations in 2D models persist as vertical oscillations when spatial

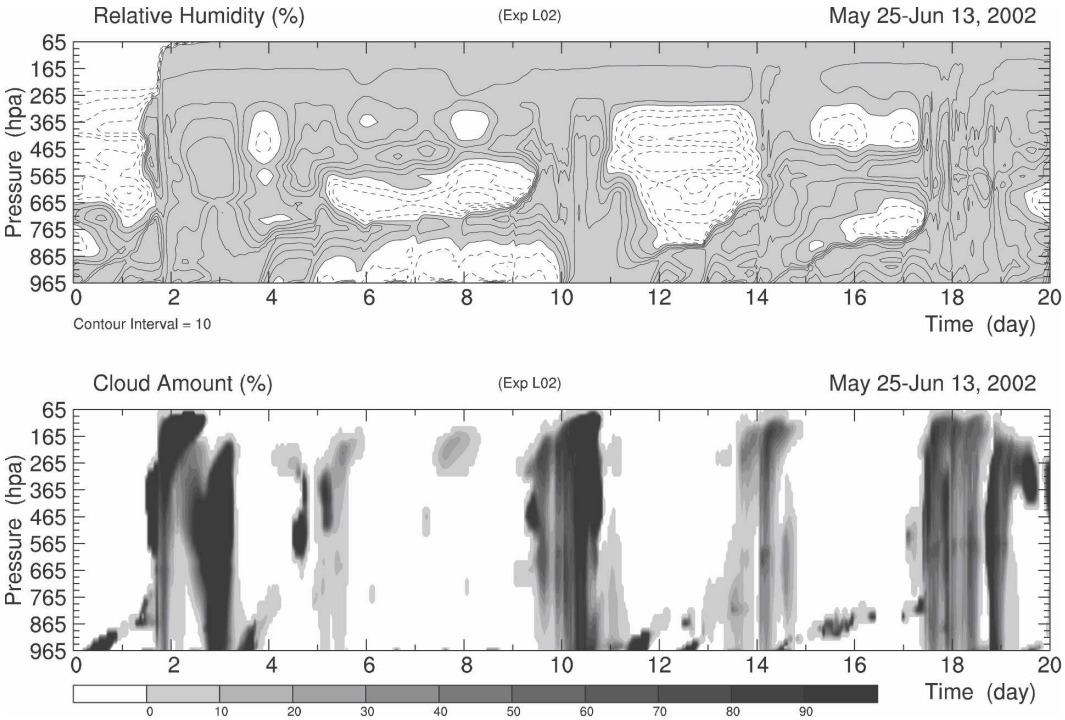

FIG. 21. Same as in Fig. 18, but for the 2002 case and experiment L02.

smoothers are weak but damp when spatial smoothers are strong. In brief, vertical oscillations are sensitive to spatial smoothers in 2D CRMs but not in 3D ones.

Strong vertical oscillations can influence precipitation and clouds through cloud microphysics. Common sense suggests that strong vertical oscillations can bring about precipitation fluctuations. It is also understandable how strong vertical oscillations influence clouds in the upper troposphere. Consider an air parcel in the upper troposphere that is saturated with respect to ice, and assume that ice falls out immediately as precipitation once deposition occurs. The parcel oscillates vertically. When the parcel moves upward and becomes supersaturated, vapor deposits into ice, which then falls out of the parcel. When the parcel returns to its original place, it becomes unsaturated, resulting in little ice aloft. This dehumidification mechanism illustrates the influence of strong vertical circulations on cloud residues. With this idealized case for perspective, it is not difficult to understand the sensitivity of clouds to vertical oscillations through cloud microphysics in 2D CRMs.

Since vertical oscillations are inversely related to spatial smoothers, it is to be expected that there would be a sensitivity of precipitation and clouds to spatial smoothers through cloud microphysics in 2D CRMs. In contrast, buoyancy damping is insensitive to spatial smoothers in 3D CRMs. Thus, cloud sensitivity in 3D CRMs is not expected. Such analysis is supported by the fact that clouds and precipitation in 3D CRMs are not sensitive to spatial smoothers like those in 2D.

The present sensitivity analysis is not contrary to previous simulations. When spatial smoothers are strong in a 2D CRM, vertical oscillations are weak and cloud residues remain in the upper troposphere, just as in its 3D counterpart, which agrees with the simulations of Grabowski et al. (1998), Tompkins (2000), and Khairoutdinov and Randall (2003). When spatial smoothers are weak in a 2D CRM, vertical oscillations persist and reduce clouds in the upper troposphere in contrast to its 3D counterpart, which agrees with the simulations of Donner et al. (1999) and Phillips and Donner (2006). This analysis also provides an explanation for the simulation of Petch and Gray (2001) on the sensitivity of clouds to dimensionality through cloud microphysics.

c. 3D CRM evaluation

Just as discussed in the preceding subsection, precipitation and clouds are sensitive to spatial smoothers in 2D CRMs. Since subgrid turbulence parameterization and sponge layers are highly uncertain factors as spatial smoothers, 2D CRM evaluations may vary from model to model and even from case to case (e.g., Phillips and Donner 2006). Therefore, 3D CRM evaluations cannot be substituted with 2D CRM evaluations.

Previous 3D CRM simulations were usually evalu-

ated with water vapor observations, showing that 3D models produced high mean relative humidity in the upper troposphere (e.g., Grabowski et al. 1998; Donner et al. 1999; Petch and Gray 2001). By tuning model parameters, 2D CRMs can be made to reduce the relative humidity so that their modeled value is close to observations (see section 3b for details). However, such parameter tuning is not advocated since artificial vertical oscillations are introduced in 2D CRMs (see the preceding subsection for details).

With the ARM cloud observations, it is possible to evaluate cloud microphysics in 3D CRMs. The present evaluation shows that modeled ice and liquid water contents are larger and smaller than observations, respectively. This result agrees with the parallel work of Zipser et al. (2006, personal communication) on the evaluation of 3D tropical cloud simulations. That model evaluation also shows that ice persists in the upper troposphere in 3D CRM simulations, which clearly effects radiation even though the ice content is very small.

6. Conclusions

Two 20-day, continental midlatitude cases are simulated with a CRM. Their results are analyzed with the aid of ARM observations and the theory on buoyancy damping to reach the following conclusions:

- Analytical solutions of a dry model exhibit the sensitivity of buoyancy damping to dimensionality. In a 3D dry model, buoyancy damps mainly because of gravity waves, and thus buoyancy damping is insensitive to friction. In a 2D model, however, buoyancy damps as a result of friction, and thus buoyancy damping is sensitive to friction.
- Differences in buoyancy damping between 2D and 3D CRMs can result in differing vertical oscillations that in turn lead to differences in the modeled precipitation and clouds through cloud microphysics, which explains the current conflicting conclusions on the sensitivity of clouds to dimensionality (see section 1c for details). Such a connection between buoyancy damping and cloud modeling is supported by the present simulations and is not contrary to previous simulations.
- Comparisons of 2D and 3D CRM simulations show that water aloft in the 2D CRM, even though it is more than observed, is spuriously reduced because of relatively strong vertical oscillations. Comparing 3D simulations to cloud observations indicates that modeled liquid water and ice are smaller and larger than observed, respectively. Moreover, modeled water vapor is larger than observed.
- Surface fluxes from LIS, a land data assimilation system, are compared with the ARM data. The LIS fluxes agree with the ARM data in general, but differ over a period. When LIS surface fluxes replace ARM data in the CRM simulations, similar results are obtained except that LIS brings about a better simulation of diurnal cloud variation in the lower troposphere. This work suggests that ARM and LIS surface flux data should be compared further with more cases in the future.

Acknowledgments. The GCE model is mainly supported by the NASA Headquarters Atmospheric Dynamics and Thermodynamics Program and the NASA Tropical Rainfall Measuring Mission (TRMM). The authors are grateful to Dr. R. Kakar at NASA headquarters for his support of this research. The research was also supported by the Office of Science (BER), U.S. Department of Energy, Interagency Agreement Number DE-AI02-04ER63755, and NASA AIST. Additional support is provided by NSF and the DOE ARM program to the Stony Brook University. Dr. Xie, working at LLNL, was supported under the auspices of the U.S. Department of Energy Office of Science, Biological and Environmental Research, by the University of California Lawrence Livermore National Laboratory under Contract W-7405-Eng-48.

The authors acknowledge the NASA Goddard Space Flight Center for computer time used in this research. They appreciate Dr. Yali Luo for providing the code to compute radar reflectivity from model mixing ratios of water species. They thank three anonymous reviewers for their critical yet constructive comments.

APPENDIX

Dimensionality Sensitivity of Buoyancy Damping in a Dry Atmosphere

In this appendix, linear 3D and 2D models are analyzed to study the sensitivity of buoyancy damping to dimensionality in an irrotational dry atmosphere, providing a means to understand buoyancy damping in a moist atmosphere. The 3D linear dry model is described as

$$\partial_t(\rho u) = -\partial_x p' + \mu\partial_{zz}^2(\rho u) \tag{A.1a}$$

$$\partial_t(\rho v) = -\partial_y p' + \mu\partial_{zz}^2(\rho v) \tag{A.1b}$$

$$\partial_t(\rho\theta') + N^2 g^{-1}\bar{\theta}\rho w = 0 \tag{A.1c}$$

$$\partial_x(\rho u) + \partial_y(\rho v) + \partial_z(\rho w) = 0 \tag{A.1d}$$

$$\partial_z p' = g\rho\theta'/\bar{\theta} \tag{A.1e}$$

in the Cartesian coordinate system (x, y, z), where (u, v, w) are the three components of the velocity vector; ρ is air density; p' and θ' denote pressure and potential temperature perturbations, respectively; N is the Brunt–Väisälä frequency; μ is a friction coefficient; and g is the acceleration due to gravity. Different from the analytical model of Bretherton and Smolarkiewicz (1989), the preceding one takes account of friction for the relative importance of gravity waves and friction in buoyancy damping.

For simplicity, N and μ are assumed to be constant in the troposphere. All variables are expanded vertically in Fourier series as

$$\{\rho u, p'\} = \sum_{m=1}^{\infty} \{(\rho u)_m, p'_m\} \cos \frac{m\pi}{H} z \tag{A.2a}$$

$$\{\rho w, \rho\theta'\} = \sum_{m=1}^{\infty} \{(\rho w)_m, (\rho\theta')_m\} \sin \frac{m\pi}{H} z, \tag{A.2b}$$

where a symbol with the subscript m denotes a coefficient of its corresponding variable; $z = 0$ and H represent the height of the surface and the tropopause, respectively. Substituting the preceding equation into (A.1) and then eliminating $(\rho w)_m$ and $(\rho\theta')_m$ yields

$$\partial_t(\rho u)_m = -\partial_x p'_m - \mu N^2 c_m^{-2}(\rho u)_m \tag{A.3a}$$

$$\partial_t(\rho v)_m = -\partial_y p'_m - \mu N^2 c_m^{-2}(\rho v)_m \tag{A.3b}$$

$$\partial_t p'_m + c_m^2[\partial_x(\rho u)_m + \partial_y(\rho v)_m] = 0, \tag{A.3c}$$

where $c_m = HN/m\pi$ is the gravity wave phase speed. If $H \sim 12$ km and $N \sim 1.2 \times 10^{-2}\ \mathrm{s}^{-1}$, then $c_m \approx 46, 23, 15,$ and $11\ \mathrm{m\,s}^{-1}$ when the vertical wavenumber $m = 1, 2, 3,$ and 4, respectively.

Differentiating (A.3a) with respect to x and (A.3b) with respect to y, and then summing the two equations and substituting (A.3c) into the resulting equation yields a pressure equation. Since a pressure perturbation is related to a temperature perturbation by $Np'_m/c_m = -g(\rho\theta')_m/\bar{\theta}$, the pressure equation is changed to a temperature equation, or

$$\partial_{tt}^2(\rho\theta')_m + \mu N^2 c_m^{-2}\partial_t(\rho\theta')_m - c_m^2[\partial_{xx}^2(\rho\theta')_m + \partial_{yy}^2(\rho\theta')_m] = 0, \tag{A.4}$$

which describes the buoyancy damping in the 3D linear model. Since the preceding equation is linear, the superposition principle is suitable. In the following paragraphs, a special case is discussed to illustrate buoyancy damping without loss of generality.

Consider the initial bell-shaped temperature perturbation

$$(\rho\theta')_m|_{t=0} = \frac{(\rho\theta^*)_m a^4}{(a^2 + x^2)(a^2 + y^2)} \tag{A.5a}$$

$$\partial_t(\rho\theta')_m|_{t=0} = 0 \tag{A.5b}$$

with $-\infty < x < +\infty$ and $-\infty < y < +\infty$, where the constant a represents the horizontal scale of the perturbation. The preceding temperature perturbation initiates gravity waves and the waves propagate outward, leading to buoyancy damping. To simplify the analysis of buoyancy damping, the following dimensionless variables are introduced

$$\hat{x} = x/a$$
$$\hat{y} = y/a$$
$$\hat{t} = tc_m/a$$
$$\hat{\theta}_m = (\rho\theta')_m/(\rho\theta^*)_m$$
$$\hat{\mu} = aN^2\mu/2c_m^3.$$

With the aid of Fourier transform, Eqs. (A.4) and (A.5) are solved with

$$\hat{\theta}_m(\hat{x}, \hat{y}, \hat{t}) = \mathrm{Re}\int_0^{+\infty}\int_0^{+\infty} \frac{1}{\omega_2 - \omega_1} e^{-(|\xi|+|\eta|)} \times (\omega_2 e^{\omega_1\hat{t}} - \omega_1 e^{\omega_2\hat{t}}) e^{-i(\xi\hat{x}+\eta\hat{y})}\, d\xi\, d\eta, \tag{A.6}$$

where the operator Re chooses the real part from a complex expression and

$$\omega_{1,2} = -\hat{\mu} \pm \sqrt{\hat{\mu}^2 - (\xi^2 + \eta^2)}. \tag{A.7}$$

After setting $\xi = r\cos\alpha$ and $\eta = r\sin\alpha$, the solution (A.6) is expressed as

$$\hat{\theta}_m = \int_0^{\hat{\mu}}\int_0^{\pi/2} e^{-r(\cos\alpha+\sin\alpha)-\hat{\mu}\hat{t}}\left[\cosh\left(\hat{t}\sqrt{\hat{\mu}^2 - r^2}\right) + \hat{\mu}\frac{\sinh\left(\hat{t}\sqrt{\hat{\mu}^2 - r^2}\right)}{\sqrt{\hat{\mu}^2 - r^2}}\right] r\cos[r(\hat{x}\cos\alpha + \hat{y}\sin\alpha)]\, d\alpha\, dr$$
$$+ \int_{\hat{\mu}}^{+\infty}\int_0^{\pi/2} e^{-r(\cos\alpha+\sin\alpha)-\hat{\mu}\hat{t}}\left[\cos\left(\hat{t}\sqrt{r^2 - \hat{\mu}^2}\right) + \hat{\mu}\frac{\sin\left(\hat{t}\sqrt{r^2 - \hat{\mu}^2}\right)}{\sqrt{r^2 - \hat{\mu}^2}}\right] r\cos[r(\hat{x}\cos\alpha + \hat{y}\sin\alpha)]\, d\alpha\, dr. \tag{A.8}$$

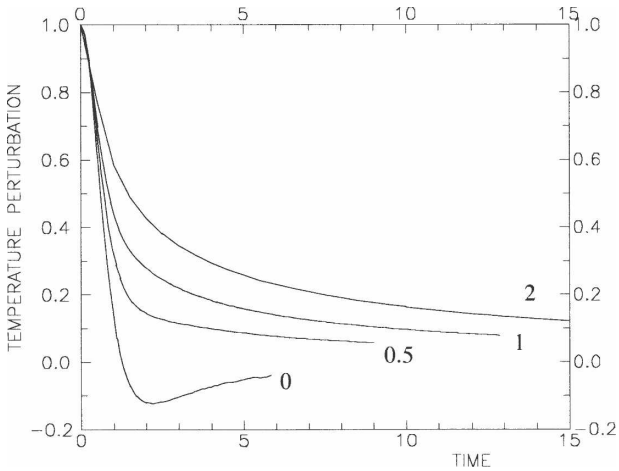

FIG. A1. The potential temperature perturbation vs time $\hat{\tau}$ at $\hat{x} = \hat{y} = 0$. The numbers beside the lines indicate the dimensionless friction coefficient $\hat{\mu}$.

Figure A1 displays the potential temperature perturbation versus $\hat{t}$ at $\hat{x} = \hat{y} = 0$, showing buoyancy damping with time.

Equation (A.8) can be used to understand buoyancy damping in a 3D model. Since the second term on the right-hand side of (A.8) effectively has the factor $\exp(-\hat{\mu}\hat{t})$ in the integrand while the first one does not [or $\cosh(\hat{\mu}\hat{t})$ cancels $\exp(-\hat{\mu}\hat{t})$ in the first term], the first and the second terms dominate when $\hat{\mu}\hat{t} \gg 1$ and $\hat{\mu}\hat{t} \ll 1$, respectively. In other words, the two terms alternate in their relative importance when $\hat{t}$ increases for a given $\hat{\mu}$, implying that buoyancy damping consists of two stages. In the first stage, an initial temperature perturbation propagates outward and the temperature perturbation at the origin decreases with time. The amplitude of the temperature perturbation decreases with time because the perturbation is distributed into a wider area. In the second stage, the perturbation dissipates due to friction in the wider area. Hence, when $\hat{\mu}$ is very small, the amplitude of the temperature perturbation decreases mainly in the first stage, and therefore, the decrease of the perturbation amplitude is almost independent of friction.

A 2D linear dry model is discussed next to show the sensitivity of buoyancy damping to dimensionality. The 2D model is the same as the 3D model in (A.1) except there is no y direction. Following the same steps from (A.1) to (A.4), the buoyancy damping in the 2D model is described as

$$\partial_{tt}^2(\rho\theta')_m + \mu N^2 c_m^{-2}\partial_t(\rho\theta')_m - c_m^2\partial_{xx}^2(\rho\theta')_m = 0. \quad \text{(A.9)}$$

Since the preceding wave equation is one-dimensional in nature, temperature perturbations (or buoyancy) in the 2D model do not damp with time when the atmosphere is inviscid. In other words, buoyancy in a 2D model damps only due to friction, which is quite different from that in its corresponding 3D model. In summary, 2D buoyancy damping is sensitive to friction, but 3D buoyancy damping is not.

REFERENCES

Ackerman, T. P., and G. M. Stokes, 2003: The Atmospheric Radiation Measurement Program. *Phys. Today,* **56,** 38–44.

Albrecht, B., and S. K. Cox, 1975: The large-scale response of the tropical atmosphere to cloud-modulated infrared heating. *J. Atmos. Sci.,* **32,** 16–24.

Bretherton, C. S., and P. K. Smolarkiewicz, 1989: Gravity waves, compensating subsidence and detrainment around cumulus clouds. *J. Atmos. Sci.,* **46,** 740–759.

Brown, P. R. A., and A. J. Heymsfield, 2001: The microphysical properties of tropical convective anvil cirrus: A comparison of model and observations. *Quart. J. Roy. Meteor. Soc.,* **127,** 1535–1550.

Cess, R. D., and Coauthors, 1990: Intercomparison and interpretation of climate feedback processes in 19 atmospheric general circulation models. *J. Geophys. Res.,* **95,** 16 601–16 615.

Clothiaux, E. E., T. P. Ackerman, G. G. Mace, K. P. Moran, R. T. Marchand, M. A. Miller, and B. E. Martner, 2000: Objective determination of cloud heights and radar reflectivities using a combination of active remote sensors at the ARM CART sites. *J. Appl. Meteor.,* **39,** 645–665.

Cosgrove, B. A., and Coauthors, 2003: Real-time and retrospective forcing in the North American Land Data Assimilation System (NLDAS) project. *J. Geophys. Res.,* **108,** 8842, doi:10.1029/2002JD003118.

Dong, X., and G. G. Mace, 2003: Profiles of low-level stratus cloud microphysics deduced from ground-based measurements. *J. Atmos. Oceanic Technol.,* **20,** 42–53.

Donner, L. J., C. J. Seman, and R. S. Hemler, 1999: Three-dimensional cloud-system modeling of GATE convection. *J. Atmos. Sci.,* **56,** 1885–1912.

Emanuel, K. A., 1995: The behavior of a simple hurricane model using a convective scheme based on subcloud-layer entropy equilibrium. *J. Atmos. Sci.,* **52,** 3960–3968.

——, 1999: Thermodynamic control of hurricane intensity. *Nature,* **401,** 665–669.

——, and D. J. Raymond, 1993: *The Representation of Cumulus Convection in Numerical Models. Meteor. Monogr.,* No. 46, Amer. Meteor. Soc., 246 pp.

Grabowski, W. W., 2001: Coupling cloud processes with the large-scale dynamics using the cloud-resolving convection parameterization (CRCP). *J. Atmos. Sci.,* **58,** 978–997.

——, X. Wu, M. W. Moncrieff, and D. Hall, 1998: Cloud-resolving modeling of cloud systems during Phase III of GATE. Part II: Effects of resolution and the third spatial dimension. *J. Atmos. Sci.,* **55,** 3264–3282.

Hansen, M. C., R. S. DeFries, J. R. G. Townshend, and R. Sohlberg, 2000: Global land cover classification at 1km spatial resolution using a classification tree approach. *Int. J. Remote Sens.,* **21,** 1331–1364.

Heymsfield, A. J., and L. J. Donner, 1990: A scheme for parameterizing ice-cloud water content in general circulation models. *J. Atmos. Sci.,* **47,** 1865–1877.

——, and J. Iaquinta, 2000: Cirrus crystal terminal velocities. *J. Atmos. Sci.,* **57,** 916–938.

Hong, S.-Y., J. Dudhia, and S.-H. Chen, 2004: A revised approach to ice microphysical processes for the bulk parameterization of clouds and precipitation. *Mon. Wea. Rev.,* **132,** 103–120.

Johnson, D. E., W.-K. Tao, J. Simpson, and C.-H. Sui, 2002: A study of the response of deep tropical clouds to large-scale thermodynamic forcing. Part I: Modeling strategies and simulations of TOGA COARE convective systems. *J. Atmos. Sci.,* **59,** 3492–3518.

Khairoutdinov, M. F., and D. A. Randall, 2001: A cloud-resolving model as a cloud parameterization in the NCAR Communicate Climate System Model: Preliminary results. *Geophys. Res. Lett.,* **28,** 3617–3620.

——, and ——, 2003: Cloud resolving modeling of the ARM summer 1997 IOP: Model formulation, results, uncertainties, and sensitivities. *J. Atmos. Sci.,* **60,** 607–625.

——, ——, and C. DeMott, 2005: Simulation of the atmospheric general circulation using a cloud-resolving model as a superparameterization of physical processes. *J. Atmos. Sci.,* **62,** 2136–2154.

Klemp, J. B., and R. B. Wilhelmson, 1978: The simulation of three-dimensional convective storm dynamics. *J. Atmos. Sci.,* **35,** 1070–1096.

Krueger, S. K., 1988: Numerical simulation of tropical cumulus clouds and their interaction with the subcloud layer. *J. Atmos. Sci.,* **45,** 2221–2250.

Kumar, S. V., and Coauthors, 2006: Land Information System—An interoperable framework for high resolution land surface modeling. *Environ. Modell. Software,* **21,** 1402–1415.

Lesieur, M., 1990: *Turbulence in Fluids.* 2d ed. Kluwer Academic, 412 pp.

Li, X., C.-H. Sui, K.-M. Lau, and M.-D. Chou, 1999: Large-scale forcing and cloud–radiation interaction in the tropical deep convective regime. *J. Atmos. Sci.,* **56,** 3028–3042.

Lilly, D. K., 1969: Numerical simulation of two-dimensionally isotropic turbulence. *Phys. Fluids,* **12** (Suppl. II), 240–249.

Lin, Y.-L., R. D. Farley, and H. D. Orville, 1983: Bulk parameterization of the snow field in a cloud model. *J. Climate Appl. Meteor.,* **22,** 1065–1092.

Lipps, F. B., and R. S. Hemler, 1986: Numerical simulation of deep tropical convection associated with large-scale convergence. *J. Atmos. Sci.,* **43,** 1796–1816.

Liu, C., and M. W. Moncrieff, 2004: Effects of convectively generated gravity waves and rotation on the organization of convection. *J. Atmos. Sci.,* **61,** 2218–2227.

Luo, Y., S. K. Krueger, G. G. Mace, and K.-M. Xu, 2003: Cirrus cloud properties from a cloud-resolving model simulation compared to cloud radar observations. *J. Atmos. Sci.,* **60,** 510–525.

Mapes, B. E., 1993: Gregarious tropical convection. *J. Atmos. Sci.,* **50,** 2026–2037.

Miller, M. A., K. L. Johnson, D. T. Troyan, E. E. Clothiaux, E. J. Mlawer, and G. G. Mace, 2003: ARM value-added cloud products: Description and status. *Proc. 13th ARM Science Team Meeting,* Broomfield, CO, U.S. Dept. of Energy. [Available online at http://www.arm.gov/publications/proceedings/conf13/extended_abs/miller-ma.pdf.]

Moeng, C.-H., and Coauthors, 1996: Simulation of a stratocumulus-topped planetary boundary layer: Intercomparison among different numerical codes. *Bull. Amer. Meteor. Soc.,* **77,** 261–278.

Moncrieff, M. W., S. K. Krueger, D. Gregory, J.-L. Redelsperger, and W.-K. Tao, 1997: GEWEX Cloud System Study (GCSS) Working Group 4: Precipitating convective cloud systems. *Bull. Amer. Meteor. Soc.,* **78,** 831–845.

Neelin, J. D., and I. M. Held, 1987: Modeling tropical convergence based on the moist static energy budget. *Mon. Wea. Rev.,* **115,** 3–12.

Nilsson, J., and K. A. Emanuel, 1999: Equilibrium atmosphere of a two-column radiative convective model. *Quart. J. Roy. Meteor. Soc.,* **125,** 2239–2264.

Petch, J. C., and M. E. B. Gray, 2001: Sensitivity studies using a cloud-resolving model simulation of the tropical west Pacific. *Quart. J. Roy. Meteor. Soc.,* **127,** 2287–2306.

Phillips, V. T. J., and L. J. Donner, 2006: Cloud microphysics, radiation and vertical velocities in two- and three-dimensional simulations of deep convection. *Quart. J. Roy. Meteor. Soc.,* **132,** 3011–3033.

Randall, D., M. Khairoutdinov, A. Arakawa, and W. Grabowski, 2003: Breaking the cloud parameterization deadlock. *Bull. Amer. Meteor. Soc.,* **84,** 1547–1564.

Raymond, D. J., 1995: Regulation of moist convection over the west Pacific warm pool. *J. Atmos. Sci.,* **52,** 3945–3959.

——, 2000: The Hadley circulation as a radiative–convective instability. *J. Atmos. Sci.,* **57,** 1286–1297.

——, and X. Zeng, 2000: Instability and large-scale circulations in a two-column model of the tropical troposphere. *Quart. J. Roy. Meteor. Soc.,* **126,** 3117–3135.

——, and ——, 2005: Modeling tropical atmospheric convection in the context of the weak temperature gradient approximation. *Quart. J. Roy. Meteor. Soc.,* **131,** 1301–1320.

Rutledge, S. A., and P. V. Hobbs, 1984: The mesoscale and microscale structure and organization of clouds and precipitation in midlatitude clouds. XII: A diagnostic modeling study of precipitation development in narrow cold-frontal rainbands. *J. Atmos. Sci.,* **41,** 2949–2972.

Simpson, J., and W.-K. Tao, 1993: The Goddard Cumulus Ensemble model. Part II: Applications for studying cloud precipitating processes and for NASA TRMM. *Terr. Atmos. Oceanic Sci.,* **4,** 73–116.

Smolarkiewicz, P. K., and W. W. Grabowski, 1990: The multidimensional positive advection transport algorithm: Nonoscillatory option. *J. Comput. Phys.,* **86,** 355–375.

Sobel, A. H., and C. S. Bretherton, 2000: Modeling tropical precipitation in a single column. *J. Climate,* **13,** 4378–4392.

Soil Survey Staff, cited 2006: U.S. general soil map (STATSGO). Natural Resources Conservation Service, United States Department of Agriculture. [Available online at http://www.ncgc.nrcs.usda.gov/products/datasets/statsgo/index.html.]

Soong, S.-T., and Y. Ogura, 1980: Response of tradewind cumuli to large-scale processes. *J. Atmos. Sci.,* **37,** 2035–2050.

Starr, D. O., and S. K. Cox, 1985: Cirrus clouds. Part I: Cirrus cloud model. *J. Atmos. Sci.,* **42,** 2663–2681.

Swann, H., 1998: Sensitivity to the representation of precipitating ice in CRM simulations of deep convection. *Atmos. Res.,* **47–48,** 415–435.

Tao, W.-K., 2003: Goddard cumulus ensemble (GCE) model: Application for understanding precipitating processes. *Cloud Systems, Hurricanes, and the Tropical Rainfall Measuring Mission (TRMM): A Tribute to Dr. Joanne Simpson, Meteor. Monogr.,* No. 29, Amer. Meteor. Soc., 107–138.

——, and S.-T. Soong, 1986: A study of the response of deep

tropical clouds to mesoscale processes: Three-dimensional numerical experiments. *J. Atmos. Sci.,* **43,** 2653–2676.

——, and J. Simpson, 1993: The Goddard Cumulus Ensemble model. Part I: Model description. *Terr. Atmos. Oceanic Sci.,* **4,** 19–54.

——, ——, and S.-T. Soong, 1987: Statistical properties of a cloud ensemble: A numerical study. *J. Atmos. Sci.,* **44,** 3175–3187.

——, S. Lang, J. Simpson, C.-H. Sui, B. Ferrier, and M.-D. Chou, 1996: Mechanism of cloud–radiation interaction in the Tropics and midlatitudes. *J. Atmos. Sci.,* **53,** 2624–2651.

——, and Coauthors, 2003: Microphysics, radiation and surface processes in the Goddard Cumulus Ensemble (GCE) model. *Meteor. Atmos. Phys.,* **82,** 97–137.

Tompkins, A. M., 2000: The impact of dimensionality on long-term cloud-resolving model simulations. *Mon. Wea. Rev.,* **128,** 1521–1535.

——, and G. C. Craig, 1998: Radiative-convective equilibrium in a three-dimensional cloud ensemble model. *Quart. J. Roy. Meteor. Soc.,* **124,** 2073–2098.

Wakimoto, R. M., H. V. Murphey, R. G. Fovell, and W.-C. Lee, 2004: Mantle echoes associated with deep convection: Observations and numerical simulations. *Mon. Wea. Rev.,* **132,** 1701–1720.

Weckwerth, T. M., and Coauthors, 2004: An overview of the International H_2O Project (IHOP_2002) and some preliminary highlights. *Bull. Amer. Meteor. Soc.,* **85,** 253–277.

Wu, X., W. W. Grabowski, and M. W. Moncrieff, 1998: Long-term behavior of cloud systems in TOGA COARE and their interactions with radiative and surface processes. Part I: Two-dimensional modeling study. *J. Atmos. Sci.,* **55,** 2693–2714.

——, W. D. Hall, W. W. Grabowski, M. W. Moncrieff, W. D. Collins, and J. T. Kiehl, 1999: Long-term behavior of cloud systems in TOGA COARE and their interactions with radiative and surface processes. Part II: Effects of ice microphysics on cloud–radiation interaction. *J. Atmos. Sci.,* **56,** 3177–3195.

Xie, S., and Coauthors, 2005: Simulations of midlatitude frontal clouds by single-column and cloud-resolving models during the Atmospheric Radiation Measurement March 2000 cloud intensive operational period. *J. Geophys. Res.,* **110,** D15S03, doi:10.1029/2004JD005119.

Xu, K.-M., and D. A. Randall, 1996: Explicit simulation of cumulus ensembles with the GATE Phase III data: Comparison with observations. *J. Atmos. Sci.,* **53,** 3709–3736.

——, and Coauthors, 2002: An intercomparison of cloud-resolving models with the Atmospheric Radiation Measurement summer 1997 IOP data. *Quart. J. Roy. Meteor. Soc.,* **128,** 593–624.

——, and Coauthors, 2005: Modeling springtime shallow frontal clouds with cloud-resolving and single-column models. *J. Geophys. Res.,* **110,** D15S04, doi:10.1029/2004JD005153.

Zeng, X., W.-K. Tao, and J. Simpson, 2005: An equation for moist entropy in a precipitating and icy atmosphere. *J. Atmos. Sci.,* **62,** 4293–4309.

Zhang, M. H., and J. L. Lin, 1997: Constrained variational analysis of sounding data bases on column-integrated budgets of mass, heat, moisture, and momentum: Approach and application to ARM measurements. *J. Atmos. Sci.,* **54,** 1503–1524.

——, ——, R. T. Cederwall, J. J. Yio, and S. C. Xie, 2001: Objective analysis of ARM IOP data: Method and sensitivity. *Mon. Wea. Rev.,* **129,** 295–311.

——, and Coauthors, 2005: Comparing clouds and their seasonal variations in 10 atmospheric general circulation models with satellite measurement. *J. Geophys. Res.,* **110,** D15S02, doi:10.1029/2004JD005021.